

Chitosan Immobilization on Bio-MOF Nanostructures: A Biocompatible pH-Responsive Nanocarrier for Doxorubicin Release on MCF-7 Cell Lines of Human Breast Cancer

Reza Abazari,[†] Ali Reza Mahjoub,^{*,†} Farangis Ataei,^{*,‡} Ali Morsali,^{*,†} Cameron L. Carpenter-Warren,[§] Kayhan Mehdizadeh,[‡] and Alexandra M. Z. Slawin[§]

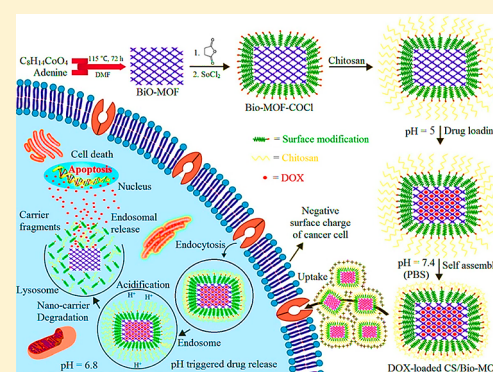
[†]Department of Chemistry, Faculty of Basic Sciences, Tarbiat Modares University, Tehran, Iran 14115-175

[‡]Department of Biochemistry, Faculty of Biological Sciences, Tarbiat Modares University, Tehran, Iran, 14115-175

[§]School of Chemistry, University of St Andrews, St Andrews, Fife, U.K. KY16 9ST

Supporting Information

ABSTRACT: In this work, a bio-metal–organic framework (Bio-MOF) coated with a monodispersed layer of chitosan (CS; CS/Bio-MOF) was synthesized and applied as a pH-responsive and target-selective system for delivery of doxorubicin (DOX) in the treatment of breast cancer. The efficiency of the nanocarrier in loading and releasing DOX was assessed at different pH levels. To monitor the in vitro drug release behavior of the drug-loaded carrier, the carrier was immersed in a phosphate buffered saline solution (PBS, pH 7.4) at 37 °C. According to the observations, the nanocarrier presents a slow and continuous release profile as well as a noticeable drug loading capacity. In addition, the carrier demonstrates a pH-responsive and target-selective behavior by releasing a high amount of DOX at pH 6.8, which is indicative of tumor cells and inflamed tissues and releasing a substantially lower amount of DOX at higher pH values. In addition, the results indicated that pH is effective on DOX uptake by CS/Bio-MOF. A 3.6 mg amount of DOX was loaded into 10 mg of CS/Bio-MOF, resulting in a 21.7% removal at pH 7.4 and 93.0% at pH 6.8. The collapsing and swelling of the CS layers coated on the surface of the Bio-MOFs were found to be responsible for the observed pH dependence of DOX delivery. Moreover, the 3-(4,5-dimethylthiazol-2-yl)-2,5-diphenyltetrazolium bromide (MTT) assay and the trypan blue test were performed on the MCF-7 (breast cancer) cell line in the presence of the CS/Bio-MOF carrier to confirm its biological compatibility. In addition, Annexin V staining was conducted to evaluate the cytotoxicity of the free and loaded DOX molecules. On the basis of the obtained optical microscopy, MTT assay, fluorescence microscopy, and dyeing results, the CS/Bio-MOF carrier greatly enhances cellular uptake of the drug by the MCF-7 cells and, therefore, apoptosis of the cells due to its biocompatibility and pH-responsive behavior.



1. INTRODUCTION

One of the current research areas of medicinal chemistry is devoted to the development of manageable and targeted drug delivery systems to deliver effective doses of medicines to the targets of interest and avoid the intrinsic drawbacks of traditional therapeutic drugs.^{1–3} To complete these two missions, several fundamental requirements should be considered in the design of drug delivery systems. The most crucial requirement is that the release of the loaded drug should be inhibited as much as possible until the carrier reaches its target location to reduce the associated side effects on healthy cells.^{4–6} Once the loaded carrier reaches the target, a specific mechanism should take place to release the drug into the targeted area in a controlled manner.^{7–9} Fulfilling this requirement is particularly essential when the loaded drug is an anticancer agent. As a DNA-damaging chemotherapeutic agent and the most well-known anticancer drug in chemotherapy, doxorubicin (DOX) has been used in the treatment of a wide range of cancers,

including ovarian, cervix, bladder, lung, leukemia, prostate, and breast cancers.^{10,11} Though DOX presents many favorable characteristics, it exhibits serious complications on intact cells, such as nephrotoxicity, cardiotoxicity, and hepatotoxicity. Along with these cytotoxic effects, DOX suppresses multiplication of tumor cells and causes cell apoptosis by restraining DNA replication and inhibiting the topoisomerase II enzyme.^{12–14} To circumvent the undesirable effects of DOX, it should be delivered to the target tumor cells directly through legitimate vectors. To this end, recent research has focused on developing the nanocarriers that can directly deliver anticancer drugs to tumors and leave healthy cells almost unaffected.^{15–17}

A mechanism for triggering drug release from a nanocarrier is pH change.^{18,19} This mechanism relies on the fact that the physiological pH is 7.4, whereas the pH of cancerous extracellular

Received: July 12, 2018

environments is significantly lower (pH 5.7–6.8).^{20–22} According to this mechanism, if the designed carrier adopts a “closed” conformation at physiological pH and forms an “open” conformation at lower pH values, it can deliver the drug to cancerous cells and protect healthy cells.^{23–25} Some examples of the inorganic materials that follow this mechanism include Fe₃O₄, mesoporous silica nanoparticles (MSNs), quantum dots, and carbon nanotubes.^{26,27} Among the outlined materials, MSNs have attracted much interest due to their tunable size, high internal surface area, and flexibility of surface modification.^{28,29} The negative point about MSNs is that, like any other silica-based nanoparticle, their dispersibility and biocompatibility are limited for bioapplications.³⁰ Furthermore, their synthesis route is multistep and is relatively complicated, which restricts practical application of MSNs. Consequently, novel biocompatible and efficient carriers should be developed to transport anticancer drugs. Another example of inorganic drug delivery tools refers to metal–organic frameworks (MOFs), which have received a great deal of attention due to their huge surface area, adjustable pore size, functionalizability, biological inertness, and adjustable properties.^{31,32} In particular, MOFs are appropriate for delivery of anticancer drugs, since their structures remain intact at physiological pH and break down at lower pH levels. In fact, acidic conditions result in the protonation of the ionic metal-linker bonds of MOFs, breakdown of their extended structures, and release of the drug to the target.³³ This mechanism of action was first elucidated by Ferey and Lin^{34–37} but inspired many other researchers to take advantage of MOFs. For instance, it motivated us to devise a MOF-based pH-responsive nanocarrier with high specific surface area and apply it to DOX delivery to the PC3 and HeLa cell lines, which led to the observation of noticeable cytotoxicity results.³⁸ An important issue is that unmodified MOFs are not intelligent and have the potential of exhibiting toxicity at high doses because of the interactions of their surfaces with cellular membranes.^{39,40} These issues can be solved by combining MOFs with biological molecules. In this respect, some biological metal–organic frameworks (Bio-MOFs) have emerged,^{41,42} in which biomolecules are integrated into the MOF structure to make it biocompatible and more suitable for biological and medicinal applications.⁴³ Though Bio-MOFs have received much attention as a result of their elegant architecture, enriched supramolecular chemistry, and biological compatibility^{44–47} and they are ideal candidates for pH-responsive drug delivery, most studies on Bio-MOFs are limited to analysis of their crystalline state due to their low water solubility.^{48,49}

To solve the solubility issue of Bio-MOFs, composites of Bio-MOFs and polymers, such as chitosan (CS), can be employed. CS is a multifunctional natural polysaccharide that is comprised of β -(1,4)-linked glucosamine and *N*-acetyl glucosamine units. This polymer is highly biodegradable, bioavailable, and nontoxic and possesses many important medicinal properties. Moreover, it can be converted to soluble polycationic salts or other derivatives to produce films, fibers, hydrogels, and other agents with suitable traits.^{50,51} In addition, protonation and deprotonation of the amino groups of CS can result in some structural changes that permit it to act as a pH-sensitive “gatekeeper”,^{52–54} which means that CS can be used to design a pH-responsive drug delivery system.⁵⁵ That is why CS has been used in biomedical contexts from drug delivery to tissue engineering.^{56–58} The main disadvantages of CS for drug delivery applications are its uncontrollable drug release profile, drug delivery before reaching the target organ, and

heterogeneous dispersion of drugs within its matrix.⁵⁹ These disadvantages can be worked out by incorporating CS onto various inorganic materials, e.g. MSNs,⁶⁰ graphene oxide,⁶¹ and organo-ruthenium complexes.⁶²

As combining both Bio-MOF and CS with an appropriate material can help to surpass the limitations of their application in drug delivery, this study proposes combining Bio-MOF and CS with each other to obtain their desirable properties and overcome their disadvantages. The resultant composite (CS/Bio-MOF) is thought to act as a pH-responsive biodegradable and nontoxic carrier that can provide (i) a great surface area and many surficial functional groups, resulting in a high degree of drug loading, (ii) sustainability in aqueous media, (iii) targeted, pH-responsive, and stable drug release in cancer cells, (iv) bioavailability, and (v) low cytotoxicity. As a model antitumor drug, DOX is loaded onto this nanocarrier through ionic pathways and hydrogen-bonding interactions. On the basis of the MTT assay results, the drug-loaded nanocarrier exhibits a cytotoxicity level higher than that of the free drug. To the best of our knowledge, this is the first research applying natural CS to block the pores of a Bio-MOF to develop controlled and targeted antitumor delivery.

2. EXPERIMENTAL SECTION

2.1. Materials and Physical Techniques. *N,N*-Dimethylformamide (DMF) was dried over 3 Å molecular sieves for 1 day, prior to use. Cobalt carbonate (CoCO₃, 48%, Aldrich), adenine (vitamin B₄, 99%, Sigma-Aldrich), thionyl chloride (SOCl₂, 99%, Merck), and succinic anhydride (98%, Merck) were used in the synthesis procedure. Deionized (DI) and doubly distilled water were utilized as the washing agent. The required phosphate-buffered saline solution (PBS, 0.01 M, pH 7.4) was prepared according to a standard procedure. Powder X-ray diffraction (PXRD) analysis, field-emission scanning electron microscopy (FE-SEM), and Fourier transform infrared spectroscopy (FT-IR) were used to characterize the crystal structure, morphology, and functional groups of the CS/Bio-MOF carrier, respectively. The samples were diluted with ethanol, dried on a silica wafer, and sputter-coated by gold prior to the FE-SEM examination. A Hitachi S-1460 instrument with 15 kV accelerating voltage was employed to obtain the FE-SEM images. For all samples, the PXRD analysis was performed using a Philips diffractometer (Model TM-1800) with a scanning angle of 1–50°, a nickel-filtered Cu *K* α radiation source ($\lambda = 1.542$ Å), 40 kV potential difference, 30 mA current, and a proportional counter detector working at a 4°/min scan rate. The UV–vis absorbance spectra of all samples were measured using a Camspec M330 UV–vis spectrophotometer (200–700 nm). The FT-IR spectra were obtained over the 400–4000 cm⁻¹ wavenumber range by a Shimadzu FT-IR spectrometer (Model Prestige 21) using the KBr disks of the samples. Ultrasonication was carried out in a SONICA-2200 EP ultrasonic bath with 40 kHz frequency.

2.2. Preparation of Cobalt Butyrate. The cobalt carbonate powder (1.19 g, 10 mmol) was suspended in 50 mL of ultrapure water. Butyric acid (12 mmol, 1.2 equiv) was added to the solution, gradually. To completely dissolve the cobalt carbonate solid, the solution was heated and mixed, simultaneously. Once cobalt carbonate was dissolved, the reaction flask was heated in an oven at 100 °C overnight to remove the residual water molecules and obtain a purple solid. Yield: 2.07 g of Co butyrate (92%). Anal. Calcd for Co(C₃H₇CO₂)₂ (with the 0.33CoO and 0.53H₂O impurities): C, 35.89; H, 5.67; N, 0.00. Found: C, 35.86; H, 5.61; N, 0.10.

2.3. Solvothermal Bio-MOF Synthesis. Through a simple approach and in the absence of any cryogenic agent, the Bio-MOFs were generated.⁶³ To be more specific, the Bio-MOFs were prepared by suspending 0.90 mmol of cobalt butyrate in 18 mL of DMF. Simultaneously, 2.70 mmol of adenine was poured into 54 mL of DMF and stirred intensely for 1 h to dissolve it completely. Then, the two solutions and 0.25 mL of pure water were placed in a 120 mL

container and heated to 115 °C at the heating rate of 1 °C/min in a temperature-controlled autoclave. The autoclave was kept at 115 °C for 72 h. The resultant purple crystalline product was washed with DMF (3 × 54 mL) and desiccated at 130 °C overnight to generate Bio-MOF-13-Co.

2.4. Stability of the Bio-MOF Crystals in PBS. A 150 mg portion of the Bio-MOF-13-Co sample was immersed in 10 mL of PBS in a 20 mL glass vial and shaken rigorously. After 48 h, the PXRD pattern of the humid Bio-MOFs was recorded. The Bio-MOF-13-Co samples were immersed in PBS for 48 h and then dried under an argon flow for the FE-SEM and PXRD analyses.

2.5. Acyl Chlorination of Bio-MOF (Bio-MOF-COCl). Ultrasonication for 6 h was used to disperse 80 mg of the synthesized Bio-MOF-13-Co in 8 mL of acetone at room temperature. Next, succinic anhydride (3.2 mL, 1.8 M) was gradually added to the acetone solution and the resultant solution was stirred continuously for 48 h at 4000 rpm and room temperature. The obtained suspension of Bio-MOF-COOH was centrifuged for 5 min, and the precipitate was rinsed using double-distilled water (5 × 15 mL) and ethanol (3 × 10 mL) to eliminate the residual solvent molecules. Then, 67 mg of Bio-MOF-COOH was reacted with excess SOCl₂ (7 mL) for 20 h in a desiccator at 80 °C. After that, the unreacted SOCl₂ molecules were eliminated under vacuum and Bio-MOF-COCl (63 mg) was produced.

2.6. Preparation of the Chitosan-Capped Bio-MOF (CS/Bio-MOF) Nanostructures. The synthesized Bio-MOF-COCl was coated with CS to generate a pH-responsive polyelectrolyte layer. In this respect, 1.5 g of CS was added to an aqueous solution of acetic acid (5 wt %, 150 mL) and stirred for 24 h at room temperature to obtain a bright CS solution (1% w/v). In parallel, 0.1 g of Bio-MOF-COCl and 0.22 g of sodium dodecyl sulfate were added to 15 mL of ethanol and 0.25 mL of acetic acid was added to adjust the pH level of the solution to 6–6.5. Then, the Bio-MOF-COCl solution was ultrasonicated for 2 h. Next, 25 mL of the bright CS solution was added to it and mixed for 48 h at room temperature to generate the chitosan-capped Bio-MOF (CS/Bio-MOF) composite. Finally, 0.187 g of CS/Bio-MOF was obtained by centrifugation at 2500 rpm, washed with deionized water (3 × 15 mL) and ethanol (3 × 10 mL), and dried in air.

2.7. Drug Loading and Release under in Vitro pH-Controlled Conditions. DOX was considered as a model drug for the drug-loading and release tests. The two pH values of 6.8 and 7.4 were used to simulate the conditions of cancerous and healthy cells, respectively. To load DOX, 10 mg of CS/Bio-MOF was added to an aqueous solution of DOX (10 mL, 1.0 mg mL⁻¹) at 30 °C in the dark and stirred for 8 h (three times). Then, the obtained DOX-loaded CS/Bio-MOF (DOX@CS/Bio-MOF) was collected by 4 min of centrifugation at 3000 rpm and rinsed with PBS to remove the surface physisorbed DOX molecules. To determine the extent of drug loading, the supernatant of the centrifuged solution was collected and subjected to UV/vis spectrophotometry at 482 nm. In order to specify the concentration of the drug, the recorded absorption intensity was compared with a calibration curve that was plotted for free DOX. Furthermore, the interaction of DOX with the nanocarrier was assessed by comparing the UV spectra of pure DOX with the DOX-loaded nanocarrier. The following equations were used to calculate the drug loading content (DLC, eq 1) and efficiency (DLE, eq 2) of the nanocarrier:

$$\begin{aligned} \text{drug loading content (DLC)} \\ = \left[\frac{\text{amount of DOX in carrier}}{\text{amount of DOX-loaded carriers}} \right] \times 100\% \end{aligned} \quad (1)$$

$$\begin{aligned} \text{drug loading efficiency (DLE)} \\ = \left[\frac{\text{amount of DOX in carrier}}{\text{amount of DOX for carrier preparation}} \right] \times 100\% \end{aligned} \quad (2)$$

The in vitro release tests were carried out at atmospheric pressure by compressing the DOX@CS/Bio-MOF in the form of a disk (0.12 g, *d* = 7 mm) and then sealing the disk in a dialysis bag (molecular cutoff: 50 kDa). The dialysis bag was immersed in 5 mL of

fresh PBS and stirred at 37 °C and pH 6.8 or 7.4 to disperse the DOX@CS/Bio-MOF. In the next step, at predetermined time intervals, the solution was centrifuged for 4 min at 3000 rpm and 3 mL of the supernatant was analyzed by UV/vis spectrophotometry at 482 nm to determine the released DOX concentration. After completion of each measurement, the removed supernatant was added to the mixture to keep its volume fixed. In this study, all reported results are the average values of three measurements.

2.8. Cytotoxicity of DOX-Embedded CS/Bio-MOF. The 3-(4,5-dimethylthiazol-2-yl)-2,5-diphenyltetrazolium bromide (MTT) assay was performed to investigate cell viability. In the present research, the MCF-7 cell line was selected to study the biocompatibility and in vitro cytotoxicity of free DOX, CS/Bio-MOF, and DOX@CS/Bio-MOF. In this respect, 10 levels of concentration were considered for each sample. The MCF-7 cells with the density of 10000 cells/well were seeded in 96-well plates and cultured for 24 h at 37 °C under a moist atmosphere including 5% CO₂. The media of the plates were then removed, and the cells were processed with a fresh medium (100 μL) containing various concentrations of free DOX, CS/Bio-MOF, or DOX@CS/Bio-MOF at pH 7.4 or 6.8. After 48 h of incubation, 20 μL of a MTT solution (5.0 mg mL⁻¹) was added to each well and the plates were further incubated for 4 h at 37 °C. Then, the well supernatants were removed, 150 μL of DMSO was added to each well, and the absorption of the resultant well contents was monitored at 570 nm. The recorded data are expressed as mean value ± standard deviation (SD).

2.9. Cell Proliferation Assay. HUVECs (5 × 10⁴) were cultured in 96-well plates and various concentrations of the CS/Bio-MOF carrier, free DOX, and DOX@CS/Bio-MOF (0, 0.195, 0.39, 0.781, 1.562, 3.125, 6.25, 12.5, 25, 50, and 100 μg mL⁻¹) were added to them to suppress the growth of breast cancer cells. The cells were incubated for 24 h, and then, the surviving cells were enumerated three times by adding trypan blue.

2.10. Cell Apoptosis. Separate samples of the MCF-7 cells were incubated in solutions of free DOX, pure CS/Bio-MOF, and DOX@CS/Bio-MOF for 12 h. Once the cells were separated from the flask, 2 mL of PBS was added to them and the cell suspensions were centrifuged for 5 min at 1500 rpm. Then, the cells were rinsed to remove the cell medium. After washing and rinsing, 500 μL of 1X binding buffer was added to the cells. Since the absorbances of the utilized FITC and PI dyes overlapped, four tubes were used and the samples with 10⁵ cells per tube were poured into them to correct and adjust the overlap. The tubes included a colorless tube, one tube containing the Annexin V-FITC dye, one tube containing the PI dye, and one tube containing both FITC and PI. Accordingly, 5 μL of Annexin V-FITC was added to the second and fourth tubes before incubating them for 15 min at room temperature in the dark. After incubation, 1 mL of the 1X binding buffer solution was placed in the tubes and the tube contents were centrifuged for 5 min at 1500 rpm. Next, another 250 μL of 1X binding buffer was added to the precipitated cells and 3 μL of PI was placed in the third and fourth tubes. Absorbances of the prepared specimens were recorded immediately after PI addition.

3. RESULTS AND DISCUSSION

3.1. Characterization of the Synthesized Nanocarriers. According to the literature,⁶³ Bio-MOF-13-Co, i.e. Co₂(ad)₂(C₃H₇CO₂)₂·1.1DMF·0.6H₂O, belongs to the tetragonal space group *I*4₁/*a* (*a* = 15.79 Å, *c* = 22.33 Å and $\alpha = \beta = \gamma = 90^\circ$). In this MOF, the cobalt-adeninate-butyrate “paddle-wheel” backbones are linked to the N1, N4, and N5 atoms of the adeninate ligand to create a 3D structure so that the channels are covered by the butyl groups of the butyrate building blocks. The 3D structure of this MOF is illustrated in Figure 1.

At a given acidic pH, the amino groups of the CS chains become protonated and allow CS to be responsive to pH variations in its environment.^{64,65} This feature is important, since solid tumors have an acidic pH of 5–6.8, which is much

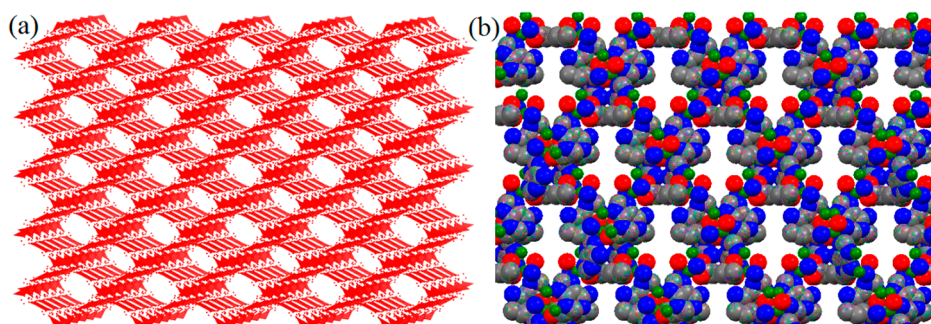


Figure 1. (a) Extended 3D structure of Bio-MOF-13-Co viewed along the *a* axis. (b) Space-filling view of Bio-MOF-13-Co along the *a* axis. The hydrogen atoms and guest molecules are omitted for clarity. Color code: O, red; N, blue; C, gray; Co, green.

lower than that of healthy tissues.^{66–68} Therefore, CS can be used as a promising biopolymer for provision of a pH-responsive polyelectrolyte layer on Bio-MOFs to control the release of the loaded anticancer drugs to the acidic local environment of tumor tissues. The FT-IR spectra of the samples obtained through synthesizing CS/Bio-MOF from the pure Bio-MOF, along with the spectrum of CS, were recorded over the range of 400–4000 cm^{-1} to verify the presence of cobalt and adenine bonds and the other functional groups. The FT-IR spectra are shown in Figure 2. Before the Bio-MOF was coated with CS,

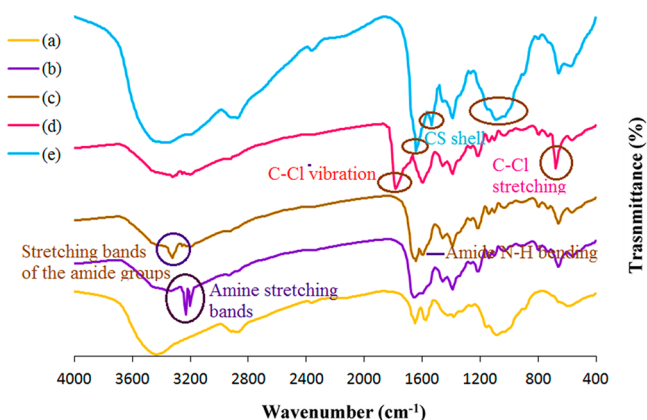


Figure 2. FT-IR spectra of chitosan (a), Bio-MOF-13-Co (b), Bio-MOF-COOH (c), Bio-MOF-COCl (d), and CS/Bio-MOF (e).

the surface functional groups of the Bio-MOF structures were manipulated using a mixture of succinic anhydride and thionyl chloride, which acted as a suitable spacer, to facilitate the reaction between the fixed CS amine groups and the flexible acyl chloride groups and form Bio-MOF-COCl. As can be seen in Figure 2, there are several low-intensity peaks from 600 to 700 cm^{-1} that are characteristic of Co–O stretching vibrations. The other peaks are altered upon different surface modifications. In Figure 2b, the FT-IR spectrum of the aminated Bio-MOF contains two weak peaks at 3211 and 3237 cm^{-1} , which are attributed to the amine stretching bands. On the other hand, in the spectrum of Bio-MOF-COOH (Figure 2c), the 1598 and 3320 cm^{-1} peaks are indicative of the N–H bending and stretching bands of the amide groups, respectively, and the broad peak at 3150 to 3550 cm^{-1} corresponds to the stretching vibration of the hydroxyl and carboxylic acid groups. In addition, in Figure 2c, the vibrational band at 1643 cm^{-1} is related to the stretching of the C=O bond of the amide groups. As a comparison of parts c and d of Figure 2 unravels, by a change of the carboxylic acid groups of the Bio-MOF-COOH to

radical chloride groups, a peak appears at 1781 cm^{-1} that could be attributed to the C–Cl vibration of the radical chloride bonds. Accordingly, the 678 cm^{-1} vibrational band refers to C–Cl stretching. Finally, when the CS shell is coated on the Bio-MOF-COCl (Figure 2e), broad peaks emerge around 1000–1150 cm^{-1} along with two new vibrational bands at 1535 and 1643 cm^{-1} , which can be ascribed to the amide I and amide II vibrations, respectively.⁶⁹

PXRD analysis was employed to determine the crystallographic properties of the synthesized samples over the 2θ range of 5–70°. The results are exhibited in Figure 3. As shown in

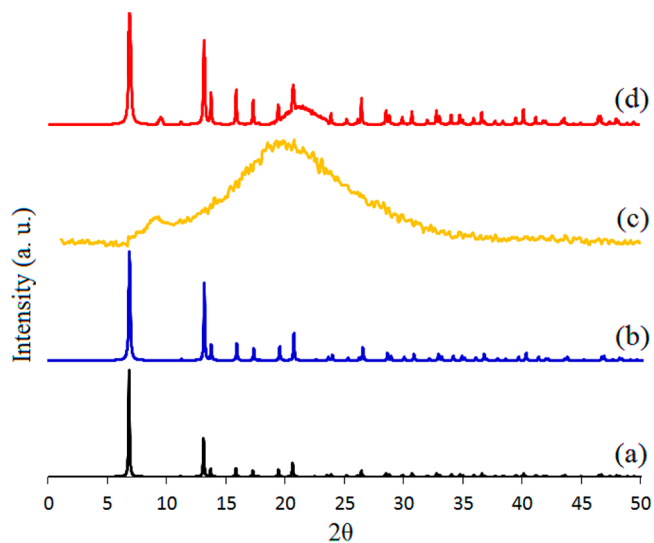


Figure 3. PXRD patterns of simulated Bio-MOF-13-Co (a), the synthesized Bio-MOF-13-Co sample (b), chitosan (c), and CS/Bio-MOF (d).

this figure, the PXRD pattern of Bio-MOF-13 (Figure 3a,b) is similar to the patterns reported by earlier studies on Bio-MOFs.⁶³ In the PXRD pattern of CS (Figure 3c), the two main peaks occur at 9.49 and 19.98° with low intensities. On the other hand, the PXRD peaks of both CS and the Bio-MOFs are preserved upon incorporation of the CS layer onto the Bio-MOF surface, in the CS/Bio-MOF composite (Figure 3d), in agreement with the FTIR data and previous studies on CS/MOFs.^{70,71}

The Bio-MOF, Bio-MOF-COOH, Bio-MOF-COCl, and CS/Bio-MOF samples were analyzed by thermal gravimetric analysis (TGA) to assess the thermal stability of their structures. In this respect, the samples were heated from room temperature to 700 °C under a nitrogen atmosphere. The TGA

curves are presented in Figure 4. According to Figure 4a, the solvent molecules adsorbed into the voids of the Bio-MOF

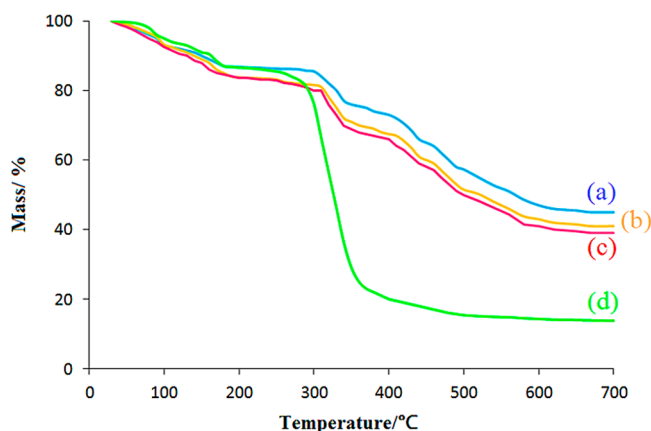


Figure 4. TGA curves of Bio-MOF-13 (a), Bio-MOF-COOH (b), Bio-MOF-COCl (c), and CS/Bio-MOF (d).

structures are lost from 30 to 100 °C and the coordinated solvent molecules are lost from 100 to 180 °C. Another weight loss occurs between 300 and 600 °C, which can be associated with the surface functional groups and the decaying scaffolds. Degradation of the organic linkers and the resultant collapse of the structures can be observed between 300 and 400 °C. In a continuation of the thermal decomposition process, at 550 °C, CoO turns into Co_3O_4 and Co_2O_3 in air.^{72,73} As can be seen in

Figure 4, the residual weights at 700 °C for Bio-MOF, Bio-MOF-COOH, and Bio-MOF-COCl are 45.2%, 41.3%, and 39.6%, respectively, which imply successful functionalization of Bio-MOF. In addition, CS/Bio-MOF was subjected to TGA analysis. On the basis of Figure 4d, the major mass loss of this composite occurs around 340 °C due to its structural decomposition. The weights lost from the Bio-MOF and CS/Bio-MOF samples are respectively 54.8% and 86.2%, which are 31.40% different and indicate the successful coating of CS.

FESEM was conducted to investigate the variations in the morphological traits of the Bio-MOFs induced by CS incorporation. The FE-SEM image and the corresponding particle size distribution histogram of Bio-MOF-13 micro-/nanostructures are displayed in parts a and b of Figure 5, respectively. On the basis of Figure 5a, the Bio-MOF-13-Co sample is composed of nanostructured crystals with octahedral morphology. While a previous study has reported sizes ranging from 2 to 10 μm for this MOF,⁶³ the Bio-MOFs synthesized in this study are noticeably smaller and their size ranges from 200 to 400 nm. Since various synthesis conditions might lead to different morphologies and particle sizes, the autoclaving and continuous heating and cooling treatments should be responsible for giving the smaller MOFs in this study. Regarding the size of the MOFs and the effect of the synthesis method, it should be noted that the synthesis route could be modified to produce smaller structures. For instance, application of ultrasonication enabled synthesis of Bio-MOF nanostructures with 30–90 nm dimension (see Figure S1). Another point is that coating the CS layer does not modify the octahedral morphology of Bio-MOF-13-Co and

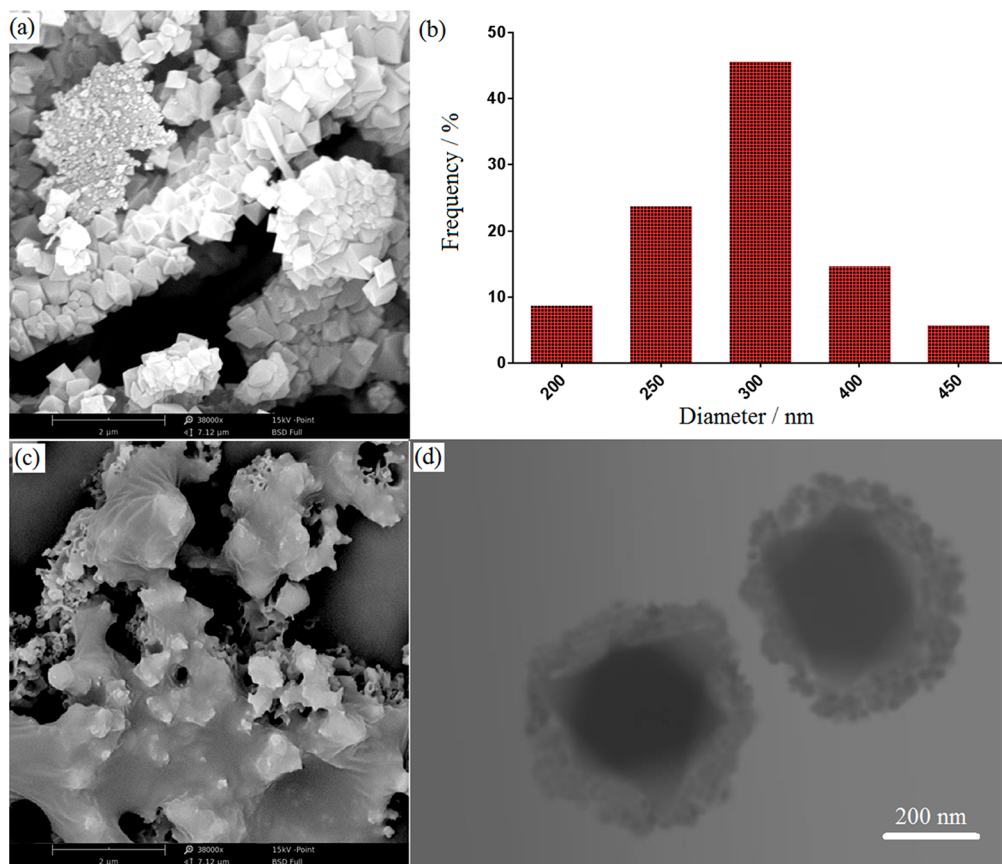


Figure 5. FE-SEM image of the Bio-MOF-13 micro-/nanostructures prepared through the hydrothermal process (a), particle size distribution histogram of the Bio-MOF-13 micro-/nanostructures (b), FE-SEM image of the Bio-MOF-13 micro-/nanostructures after chitosan incorporation (c), and a TEM image of the Bio-MOF-13 micro-/nanostructures after chitosan incorporation (d).

only results in irregular surficial agglomeration of CS and increase in size (see Figure 5c). The morphology of the Bio-MOF and CS/Bio-MOF was further studied by the TEM technique. The TEM images of the two samples are shown in Figure S2 and Figure 5d and illustrate an octahedral morphology with tough surfaces and uniform particle distributions. Moreover, Figure 5d suggests that the TEM image of the CS/Bio-MOF sample is consistent with the associated SEM result by revealing no morphological change in the Bio-MOFs upon CS deposition. In addition, this figure indicates that the CS layer has homogeneously coated the surface of the Bio-MOFs.

The ζ potential of the prepared nanocarrier was measured as a function of pH. As Figure 6 illustrates, at pH 5, the

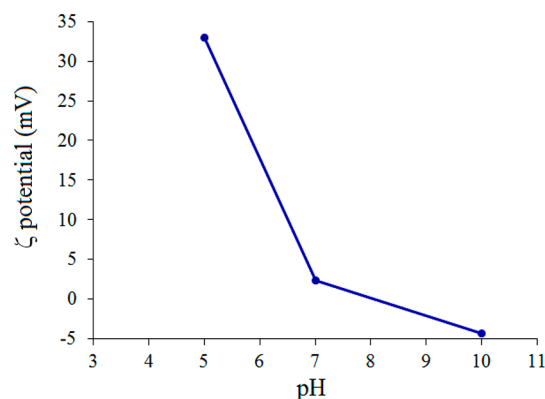


Figure 6. Effect of pH on the ζ potential of CS/Bio-MOF in water.

ζ potential of CS/Bio-MOF is +33.0 mV due to the cationic nature of the polysaccharide chains of CS, whereas the value of the ζ potential decreases to +2.4 mV at pH 7 as an outcome of CS deprotonation.⁷⁴ Finally, the ζ potential value decreases to -4.3 mV at pH 10, which can lead to a low level of electrostatic repulsion between the scaffold and the CS chains. The observed ζ potential trend indicates that CS has been successfully introduced to the Bio-MOF structure.

In addition to the FT-IR, PXRD, SEM, TEM, TGA, BET, and ζ potential analyses, ¹H NMR spectroscopy was employed to confirm successful synthesis of the CS/Bio-MOF carrier. Figure S3 displays the corresponding ¹H NMR spectra. In Figure S3a, the signals observed at 2.21 and 4.79 ppm are indicative of CS.^{75,76} On the other hand, in the ¹H NMR spectrum of CS/Bio-MOF (Figure S3b), the presence of the adenine ligand is indicated by the multiple peaks positioned at 1.75–3.75 ppm and successful grafting of CS onto the Bio-MOF structures is determined by the 0.21 ppm chemical shift that is observed for the 4.79 ppm peak of CS.

Before experiments related to the release of DOX from the prepared nanocarrier were performed, the structural stability of the nanocarrier was examined by immersing it in PBS for 1–4 days. In the meantime, the nanocarrier-PBS suspension was continuously stirred. After that, the nanocarriers were separated, dried at 60 °C, and analyzed by PXRD, FT-IR spectroscopy, and FE-SEM methods. As the PXRD patterns of Figure 7 (CS/Bio-MOF) and Figure S4 (Bio-MOF) show, the structures of the CS/Bio-MOF and Bio-MOF samples remained intact after 4 days and no impurity or additional peak appeared to indicate the occurrence of structural decomposition, only the reduction of the peak intensities after 3 days of immersion in PBS. To evaluate the shape and structural stability of the Bio-MOFs in PBS, they were also analyzed by FT-IR and

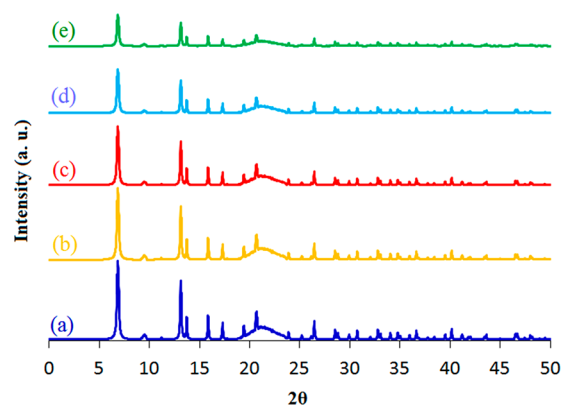


Figure 7. PXRD patterns of the as-synthesized CS/Bio-MOF (a) and CS/Bio-MOF immersed in PBS for 24 h (b), 48 h (c), 72 h (d), and 96 h (e).

FE-SEM after 48 h immersion. As can be seen in Figure S5, the FT-IR spectrum of the carriers exhibits no structural change after 48 h contact with PBS. In addition, the FE-SEM image of the carrier (Figure S6) reveals no changes in its external shape or particle size. A generalization of these results indicates that the internal structure of the carrier has been conserved while the crystallinity of the Bio-MOFs is altered slightly.

Similarly, the stability of the synthesized Bio-MOF and CS/Bio-MOF was studied in aqueous solutions. Figure S7 depicts the PXRD patterns of the two samples after 48 and 96 h of immersion in distilled water with continuous stirring at room temperature. On the basis of this figure, the Bio-MOF sample loses its structural integrity and crystallinity slightly after 4 days of immersion in aqueous solutions. Meanwhile, the CS/Bio-MOFs exhibit a higher extent of structural integrity due to the protective role of the CS coating layer, which prevents cleavage of the metal–linker bonds in the Bio-MOF structure. Therefore, all stability results show that the studied nanocarrier is stable in the aqueous environment of PBS and can be considered as a capable drug delivery system.

To further evaluate the stability of the CS/Bio-MOF carrier, its structural stability was monitored by PXRD analysis and FT-IR spectroscopy at pH 5 and 8. With respect to Figures S8 and S9, the carrier is stable at pH 6.8 for 48 h while its structure changes and decomposes gradually under highly acidic conditions. Since the pH level of cancerous cells is about 6.8, the stability of the prepared carrier was also tested at pH 6.8. According to the PXRD patterns of Figure S10, the carrier remains stable up to 3 days and then starts slowly losing its structural integrity.

3.2. Loading Doxorubicin Hydrochloride. As a conventional antitumor agent, DOX was loaded onto the Bio-MOF and CS/Bio-MOF nanocarriers to assess their drug loading and release behaviors. As stated by previous studies, drug loading and release are both influenced by a number of different interaction modes, including the covalent, hydrogen-bonding, electrostatic, and π - π interactions. Among these modes, electrostatic interactions are found to be the most significant factor⁷⁷ and are controlled by the pH of the environment. In the case of CS, since the pK_a value of CS is roughly 6.3, pH values below 6.3 result in chain protonation and a swollen, “open” CS state.^{78,79} Therefore, pH would affect the interaction of drugs with CS. In this respect, we simulated the *in vitro* loading and release behavior of DOX through changing the pH value of the *in vitro* system. When the CS/Bio-MOFs were dispersed

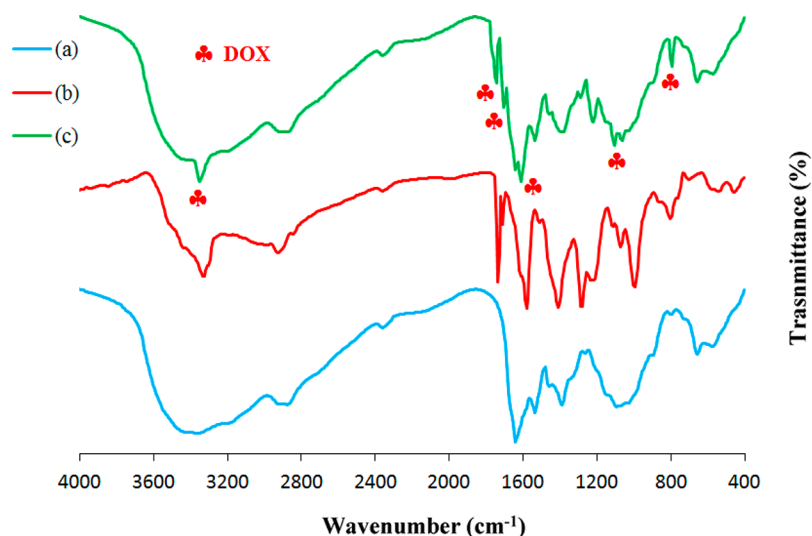


Figure 8. Comparison of the FT-IR spectra of Bio-MOF-13 (a), free DOX (b), and DOX@CS/Bio-MOF (c).

in an aqueous solution of DOX with pH 5.0, the amino groups on the surface-grafted CS chains were protonated and an extensive hydrogen-bonding network was formed. The established network helped to hold the CS chains in a swollen conformation and permitted the DOX molecules to access the Bio-MOF channels. When the pH level was increased to 8.0, the CS chains adopted a shielding “closed” conformation and hindered the loading and release of DOX. Application of UV/vis spectrophotometry and eqs 1 and 2 determined that the DLC and DLE parameters of the CS/Bio-MOF carrier are 48.1% and 92.5% while the DLC and DLE values of the Bio-MOF carrier are 39% and 76%, respectively. The greater loading for the CS/Bio-MOF carrier in comparison with Bio-MOF can be attributed to the fact that the CS chains help to adsorb more DOX drugs and result in increased loading. The successful loading of DOX into the CS/Bio-MOFs suggests that CS is a promising pH-sensitive coating material.

3.3. Proof of DOX Loading into the Nanocarriers.

Figure 8 displays the FT-IR spectra of Bio-MOF-13-Co, free DOX, and DOX@CS/Bio-MOF. In this figure, a broad band is observed at 3450 cm^{-1} that can be attributed to the O–H stretching mode of the adsorbed H_2O molecules. The broadness of this band is a consequence of extensive hydrogen bonding between the noncoordinated and coordinated H_2O molecules.⁸³ As the IR bands of DOX@CS/Bio-MOF are comprised of the vibrational modes of both DOX and the CS/Bio-MOF carrier, DOX is successfully embedded into CS/Bio-MOF (Figure 8c). To be more precise, in Figure 8c, the vibrational bands of the C=C skeleton at 1617 cm^{-1} and the C–H out-of-plane bending mode at 797 cm^{-1} are related to the aromatic rings of DOX. The band found at 1736 cm^{-1} refers to the C=O stretching mode of the aldehyde groups, while the band at 1712 cm^{-1} is associated with the C=O stretching vibrations of the unsaturated esters. The bands at 1064 and 1103 cm^{-1} correspond to the C–N stretching mode of aliphatic amines. The main changes between the vibrations of free DOX and the DOX molecules loaded into the CS/Bio-MOF carrier refer to the N–H stretching band of free DOX at 3320 cm^{-1} , which is shifted to 3347 cm^{-1} in the case of DOX@CS/Bio-MOF, and intensification of the 1598 cm^{-1} peak that is attributed to the C=O bond at the 13-keto position of DOX, in the FT-IR spectrum of the drug-loaded carrier.⁸⁴

The N_2 adsorption–desorption isotherms of the Bio-MOF structures were collected to evaluate the porosity of the synthesized Bio-MOFs. As shown in Figure 9, Bio-MOF-13-Co

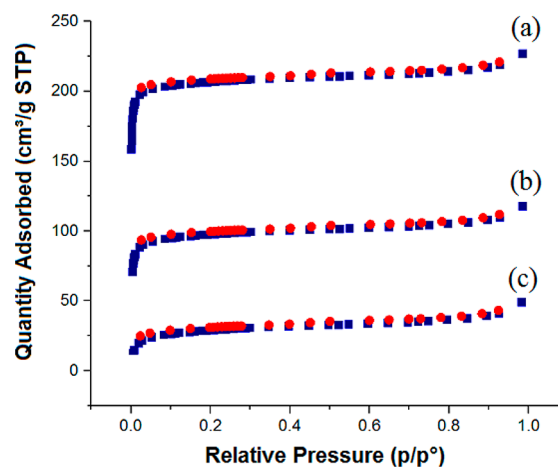


Figure 9. N_2 adsorption–desorption isotherms of Bio-MOF-13-Co (a), CS/Bio-MOF (b), and DOX@CS/Bio-MOF (c) collected at 77 K.

exhibits a type I isotherm, which is a unique feature of microporous materials. The same isotherm type is observed for CS/Bio-MOF. However, as Table S1 presents, the structural values extracted from the nitrogen adsorption curve of CS/Bio-MOF are lower than those of Bio-MOF-13 so that the BET surface area, pore volume, and pore diameter of the Bio-MOFs are respectively $935\text{ m}^2\text{ g}^{-1}$, $0.37\text{ cm}^3\text{ g}^{-1}$, and 3.47 nm and change to $438\text{ m}^2\text{ g}^{-1}$, $0.25\text{ cm}^3\text{ g}^{-1}$, and 3.12 nm after coating CS on them. These values suggest that the pore structure of Bio-MOF does not substantially change after uniform coating of CS onto its exterior surface. Therefore, the pores of the MOF can offer the space required for embedding the DOX molecules. On the other hand, the N_2 adsorption–desorption analysis shows a decrease in both the BET surface area and pore volume of the CS/Bio-MOFs after DOX loading, which confirms successful loading of the drug into the nanocarrier.

Interactions between the guest molecules and the adsorbent, i.e. DOX and CS/Bio-MOF, respectively, result in the progress

of the adsorption process. Generally, such MOF–drug interactions are weak. However, in some cases, the interactions between the host and guest molecules are noticeably stronger and lead to structural variations and chemisorption. An appropriate technique for studying such structural changes is PXRD. The PXRD pattern of the bare CS/Bio-MOFs is illustrated in Figure 10a (the red pattern), while the PXRD pattern of

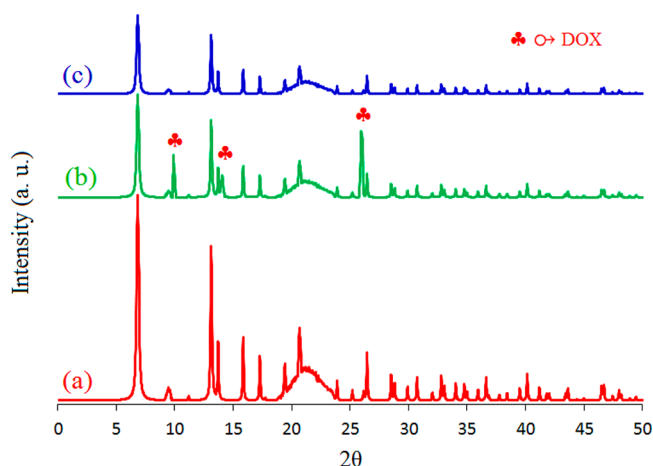


Figure 10. XRD patterns of CS/Bio-MOF before DOX loading (a) and after DOX loading (i.e., DOX@CS/Bio-MOF) (b) and the release of the loaded DOX molecules (c).

DOX@CS/Bio-MOF is shown in Figure 10b. Comparison of parts a and b of Figure 10 reveals a structural change in CS/Bio-MOF upon incorporation of DOX in spite of the well-retained crystallinity of this carrier. This change is an outcome of the interactions developed between the supramolecular drug and CS/Bio-MOF. The peaks appearing at the 2θ values of 25.96, 14.08, and 9.82° are associated with the (220), (002), and (102) Miller indices of DOX and confirm embedding of the drug into the CS/Bio-MOF matrix. This result is in line with the findings reported in the literature, as well as the FT-IR results.⁸⁵ During the dissolution test at acidic pH, the embedded DOX molecules should have been released. The corresponding PXRD pattern is displayed in Figure 10c (the blue pattern). As expected, this figure reveals no DOX-related diffraction peak and verifies successful removal of the drug.

3.4. pH-Controlled DOX Release from CS/Bio-MOF.

To explore the pH-dependent release of DOX from the CS/Bio-MOFs and simulate the physiological conditions of tumor cells and healthy body fluids, two PBS solutions with two different pH values, i.e. 6.8 and 7.4, respectively, were prepared. The concentration of DOX released from the nanocarriers into the solutions was measured by UV–vis spectrophotometry, and then, the absorbance data were used to calculate the percentage of DOX released from the carriers (Figures S11 and S12). Figure 11a exhibits the *in vitro* release profiles and demonstrates a slow growth in DOX concentration over 48 h, which means that the loaded DOX molecules are released in a continuous manner. As can be seen in Figure 11a (the red line), the release behavior of DOX@CS/Bio-MOF in the acidic PBS solution (pH 6.8) shows a significantly faster release (93% within 48 h) relative to the buffer with pH 7.4 (the blue line), which indicates just 21.7% DOX release in the first 48 h. These results reveal the dramatic effect of the pH-responsive swelling and contracting mechanism of the CS chains on DOX release. In other words, the results imply that when the drug-loaded

CS/Bio-MOFs travel under healthy cell conditions, only small amounts of DOX are released and the healthy cells are protected from the unwanted side effects of DOX. However, once the DOX-loaded CS/Bio-MOFs reach the region with a lower pH, i.e. the tumor cells, an enormous increase in the rate of DOX release happens. The release behavior of the Bio-MOFs (the yellow and green lines of Figure 11a) shows that 48.3 and 54.1% of the loaded DOX molecules are respectively released during the starting 24 h period at pH 7.4 and 6.8. Furthermore, Figure S11 displays that the loaded DOX molecules are released steadily from the Bio-MOFs over time. On the other hand, on the basis of Figure 11a, the percentages of DOX released from Bio-MOF at pH 7.4 and 6.8 after 48 h are 65.3 and 69.8%, respectively, which indicates no significant pH response. In addition, the percentage of DOX released from the Bio-MOFs is lower than that of CS/Bio-MOF at pH 6.8. The main reason behind this observation is that the DOX molecules are not only embedded within the MOF cavities but also adsorbed by the CS layer due to the positive charges generated on the amino functional groups of CS at lower pH levels.⁸⁰ To further explain this finding, one should know that CS conformations under aqueous conditions can be classified as spherical, random coil, and consolidated rods and pH is a major determining factor affecting its conformation.⁸¹ At lower pH values, the amino groups ($-\text{NH}_2$) of the CS chains become protonated ($-\text{NH}_3^+$), which improves the electrostatic repulsive potentials among the CS chains and weakens the hydrogen bonds. Consequently, the CS chains convert to a swollen polymeric matrix to lose random coils and release DOX. On the other hand, at pH 7.4, the amino groups do not possess additional positive charges, which leads to a weaker electrostatic repulsion and makes the CS chains adopt a collapsed conformation.⁸² As an outcome, diffusion of DOX and its release is hindered to a large extent. This is why, at pH 6.8, the percentage of DOX released from the CS/Bio-MOF carrier was observed to be significantly higher than that at pH 7.4. It should be noted that the CS chains act as a buffer and the CS amine groups rather than the linker units of the MOF become protonated, which means that unlike Bio-MOF, which breaks down entirely at lower pH levels and exhibits a rapid and uncontrolled DOX release behavior, CS/Bio-MOF remains largely intact and permits DOX to escape from it in a controlled fashion once it reaches the tumor. By consideration of the pH-responsive mechanism of CS/Bio-MOF, this carrier has the potential of carrying other therapeutic agents or functional molecules and presenting controlled loading and release contexts. With respect to the fact that different cellular media have various pH levels, the release of DOX was also studied at pH 5. The obtained results are displayed in Figure S13. According to this figure, the rate of DOX release from CS/Bio-MOF is significantly higher at pH 5 relative to pH 6.8. This observation can be attributed to the role of the CS layer, which forms a swollen state in acidic environments and releases more drugs at its “open” state.

Figure 11b illustrates the effect of CS content on the performance of the CS/Bio-MOF carrier. As this figure shows, the percentage of DOX released from the DOX@CS/Bio-MOFs decreases from 93 to 21.43% by an increase in the mass fraction of CS from 10% to 40%, at pH 6.8. The reason is that a high degree of cross-linking will permanently entangle the CS outer layer, reduce the swelling effect, and therefore, drastically inhibit the release of DOX from the structure when high mass fractions of CS are applied.

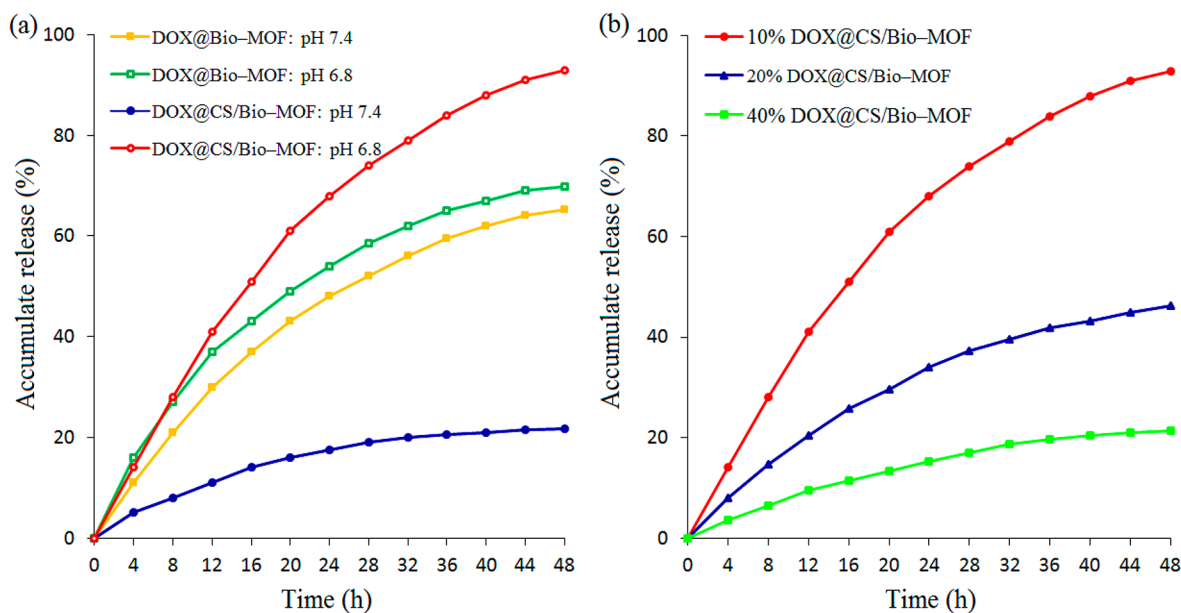


Figure 11. (a) Profiles of DOX release from the Bio-MOF and CS/Bio-MOF drug delivery systems at pH 7.4 and 6.8. (b) Profiles of DOX release from the DOX@CS/Bio-MOFs containing different chitosan:Bio-MOF mass ratios (10, 20, and 40 wt % CS), at pH 6.8.

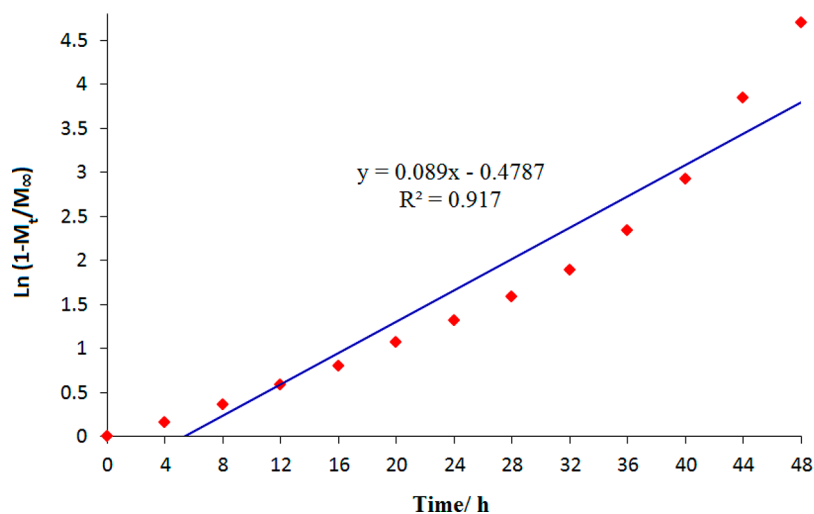


Figure 12. Kinetics of DOX release from DOX@CS/Bio-MOF in the PBS solution at pH 6.8 and at physiological temperature.

To evaluate the capability of the devised carrier in loading and releasing DOX, the performance of CS/Bio-MOF was compared with that of a physical mixture of Bio-MOF and CS (CS + Bio-MOF). The results indicated that the physical mixture does not have the potential of helping DOX loading and release so that the DLC and DLE values of CS + Bio-MOF were respectively obtained as 41 and 80.5%, which are almost close to the values related to Bio-MOF-13-Co. In addition, the release profiles of the physical mixture (Figure S14) clarified that the release of the drugs loaded onto CS + Bio-MOF is not affected by pH and the release rate remains almost the same at the two examined pH levels (6.8 and 7.4). Consequently, the physical mixture is not capable of presenting pH-responsive drug delivery.

The time profiles of DOX release from CS/Bio-MOF were fitted into several kinetics models to investigate the kinetics of the reaction. The corresponding results are presented in Figure 12 and Table S2, in which R_0 , R_1 and R_2 refer to the correlation coefficients of the zero-, first-, and second-order models,

respectively. Among these coefficients, R_1 shows the best correlation. Therefore, the studied catalytic reaction can be best described as a first-order reaction. This result also implies that the CS/Bio-MOFs conserve their scaffold integrity under the test circumstances. Since continuous desorption accounts for DOX delivery, Fick's diffusion law was applied and the fitted data were described through the single-exponential function of eq 3:

$$\ln(1 - M_t/M_\infty) = -kt \quad (3)$$

where M_t represents the release value at time t , M_∞ denotes to the maximum release value, and k indicates the first-order rate constant of drug release. According to the fitted data, the rate constant of DOX release is 0.089 h^{-1} ($R^2 = 0.917$).

Prior to evaluation of the cytotoxic effect of the synthesized samples on the MCF-7 cell line, leaching of Co from the CS/Bio-MOF structure to PBS was investigated at pH 6.8 after 24 and 48 h of contact time. This analysis was performed to distinguish the role of leached Co from that of CS/Bio-MOF in toxicifying the studied cell line. In this respect,

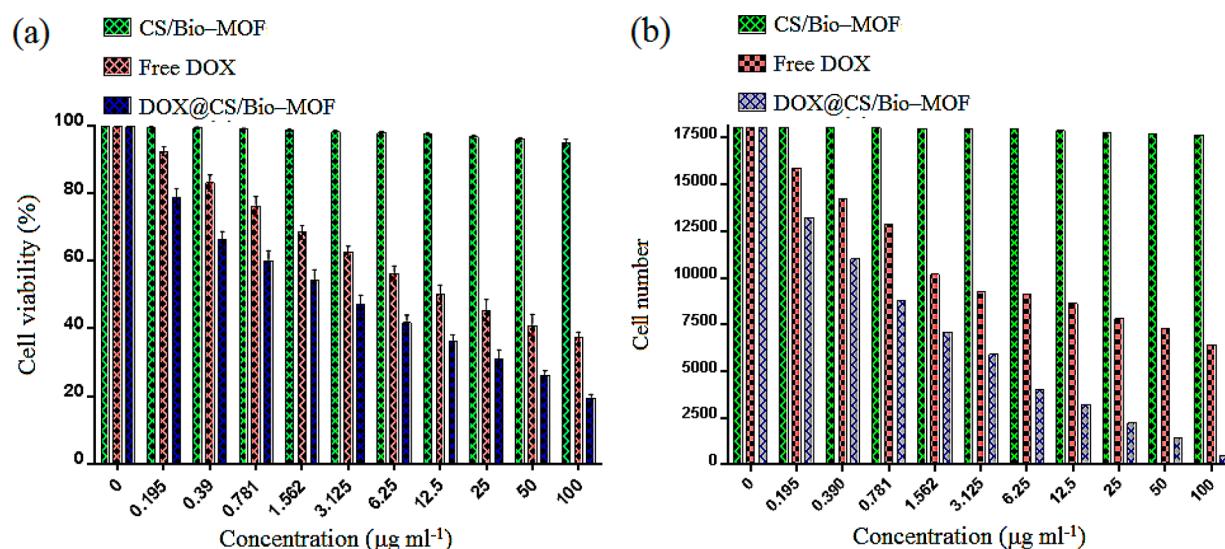


Figure 13. (a) Comparison of the cytotoxic effects of CS/Bio-MOF, DOX@CS/Bio-MOF, and free DOX on cell viability of the MCF-7 cells incubated at pH 7.4 for 24 h in the presence of various concentrations of the samples. (b) In vitro viability of the MCF-7 cells dyed with trypan blue and incubated at pH 7.4 for 24 h with various concentrations of the CS/Bio-MOF carrier, free DOX, and DOX@CS/Bio-MOF.

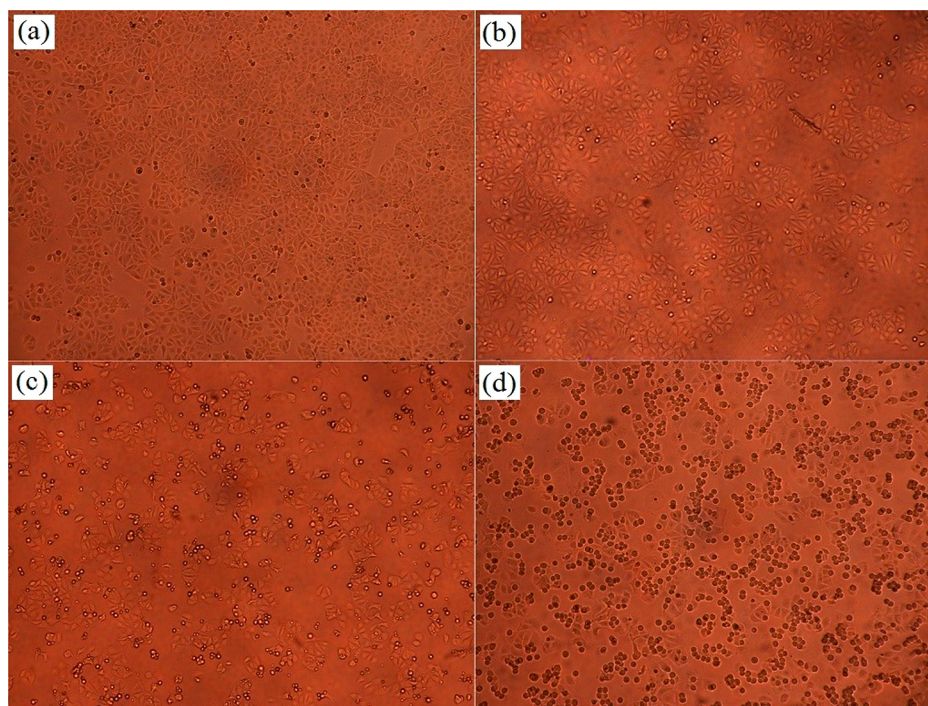


Figure 14. Morphological changes in the MCF-7 cells of the control group (a) and the cells exposed to the CS/Bio-MOF carrier (b), free DOX (c), and DOX@CS/Bio-MOF (d) at pH 7.4 for 24 h. Cell density reduction, irregular shapes, and cellular shrinkage were observed by optical microscopy.

the CS/Bio-MOFs suspended in PBS for 24 and 48 h were centrifuged and the resultant supernatant solutions were analyzed by inductively coupled plasma optical emission spectrometry (ICP-OES). This analysis determined 0.37 ppm (1.2%) and 1.15 ppm (3.75%) of Co leaching from CS/Bio-MOF at pH 6.8 after 24 and 48 h, respectively.

3.5. In Vitro Cytotoxicity by the MTT and Trypan Blue Tests. Biocompatibility of both the control CS/Bio-MOF and drug-loaded CS/Bio-MOF samples was studied by carrying out the MTT and trypan blue tests. Cell viability in the presence of different concentrations of free DOX and DOX@CS/Bio-MOF

was investigated by performing the MTT assay on the MCF-7 cell line in acidic media (pH 6.8). The obtained results are shown in Figure 13a, which exhibits a linear correlation between the concentration of both DOX@CS/Bio-MOF and free DOX with their cytotoxic impact on the examined breast cancer cells (MCF-7). As can be seen, all concentrations of DOX@CS/Bio-MOF present a significantly greater cytotoxicity relative to free DOX. The higher cytotoxicity of the drug-loaded carrier can be attributed to two main factors: first, the CS/Bio-MOF structure remains intact, which insures a controlled drug release to the target over a significant period of

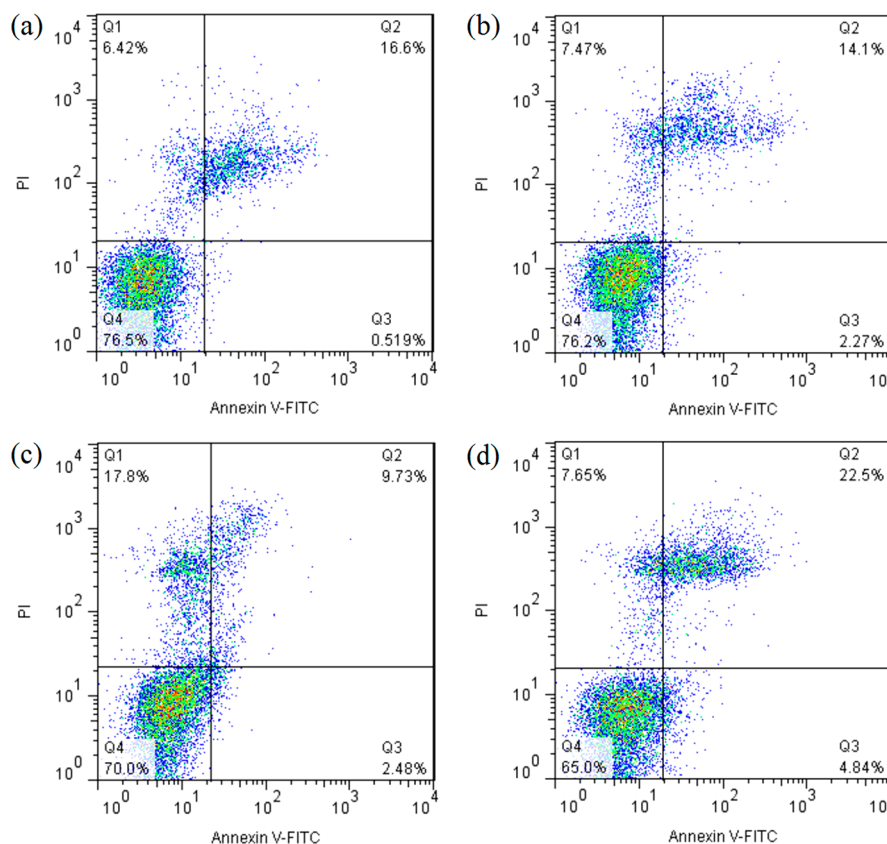


Figure 15. Flow cytometry analysis of the apoptotic and necrotic cells at pH 7.4 after 12 h incubation with the control group (a), CS/Bio-MOF (b), free DOX (c), and DOX@CS/Bio-MOF (d). The results are expressed as mean \pm standard deviation ($n = 3$). Q1–Q4 represent the necrotic, late apoptotic, early apoptotic, and live cells, respectively.

time, and second, the biocompatible nature of CS/Bio-MOF allows improved DOX uptake through the membranes of the MCF-7 cells. The same experiment was carried out at physiological pH (7.4) as a control. It was observed that the DOX-loaded CS/Bio-MOFs had no cytotoxicity at pH 7.4, even at its highest concentration ($100 \mu\text{g mL}^{-1}$). This result is consistent with the proposed mechanism and the *in vitro* studies. According to the results of MCF-7 cell viability (Figure 13a), the 50% maximal inhibitory concentration (IC_{50}) of DOX@CS/Bio-MOF is $3.125 \mu\text{g mL}^{-1}$, while the IC_{50} value of free DOX is $25 \mu\text{g mL}^{-1}$. Moreover, the CS/Bio-MOF carrier does not show any significant cytotoxic impact on the MCF-7 cells. The cell viability test was also repeated by incubating the cells with CS/Bio-MOF, DOX@CS/Bio-MOF, and free DOX for 48 h. This experimentation led to similar results (see Figure S15) and gave IC_{50} values of 6.25 and $1.562 \mu\text{g mL}^{-1}$ for the DOX-loaded MOFs and free DOX, respectively. Further, to evaluate the cytotoxicity of the CS/Bio-MOF nanocarrier, free DOX, and DOX@CS/Bio-MOF under NIR irradiation, the trypan blue test was conducted. As is shown in Figure 13b, the results of the trypan blue test are in harmony with the results of the MTT assay so that the live cell membranes do not allow entry of non-electrolyte stains into the cells whereas the dead cells are well stained.

3.6. Cellular Changes in MCF-7 after Treatment with Cytotoxic Agents. Optical microscopy images of the MCF-7 cells were prepared to assess the cellular morphology, cell viability, and membrane integrity of the MCF-7 cells as direct cytotoxicity indicators and achieve a closer mechanistic insight into the biological impacts induced by DOX@CS/Bio-MOF.

Figure 14 illustrates the obtained morphological characteristics after 24 h exposure of the MCF-7 cell line to CS/Bio-MOF, free DOX, and DOX@CS/Bio-MOF. According to this figure, the presence of $3.125 \mu\text{g mL}^{-1}$ DOX@CS/Bio-MOF causes a substantial decrease in cell density within 24 h of exposure and results in an uneven cellular shape and cellular contraction. Free DOX and CS/Bio-MOF induce similar changes, but their effect is not as considerable as that of DOX@CS/Bio-MOF. Therefore, these variations in cellular morphology and density directly indicate the cytotoxicity effect⁸⁶ of free DOX and, specifically, DOX@CS/Bio-MOF on the cell line.

Induction of apoptosis is the most prevalent method of action by most antitumor drugs.⁸⁷ In other words, the most elegant and effective strategy in cancer treatment is found to be triggering of apoptosis.⁸⁸ Therefore, the apoptotic impact of DOX@CS/Bio-MOF on the MCF-7 cell line was assessed by flow cytometry using the PI and Annexin-V FITC double-staining method. To evaluate apoptosis by flow cytometry, the MCF-7 cells were treated with $3.125 \mu\text{g mL}^{-1}$ CS/Bio-MOF, free DOX, and DOX@CS/Bio-MOF for 12 h. Figures 15 and 16 and Table 1 display the percentages of early apoptotic, late apoptotic, necrotic, and live cells present after the treatments. On the basis of the results, the MCF-7 cells exposed to DOX@CS/Bio-MOF experience a significant increase in the percentage of apoptosis (27.34%) in comparison with the cells exposed to just free DOX (12.21%). In other words, the flow cytometry results imply that DOX@CS/Bio-MOF triggers a substantially higher extent of apoptosis in the MCF-7 cells relative to free DOX.

The endocytosis capacity of the carrier was determined by incubating the MCF-7 cells with the DOX@CS/Bio-MOFs

for 6 and 12 h in the dark and following localization of the released DOX molecules in the cells' nuclei by the means of the DAPI fluorescent nuclear marker. The corresponding results are shown in Figure 17 and confirm the presence of

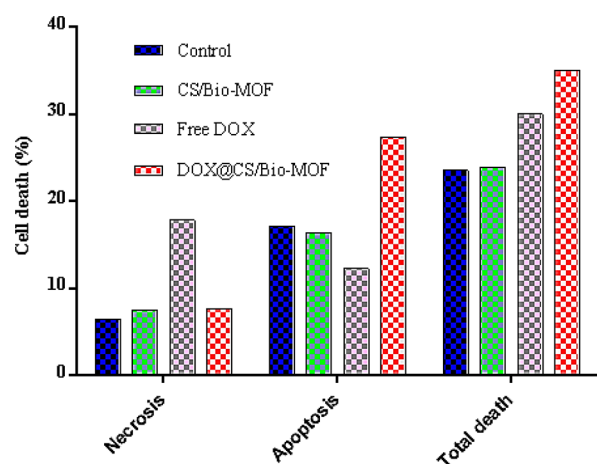


Figure 16. Quantitative necrosis, apoptosis, and death of the MCF-7 cells determined using the Annexin-V/PI dual-staining method in the framework of flow cytometry analysis at pH 7.4 ($n = 3$).

DOX in the cell nuclei by exhibiting both red (DOX) and blue (DAPI) fluorescence emissions, simultaneously. These emissions are observed after both incubation times and signify the significant endocytosis capacity of the CS/Bio-MOF carrier. The root of this observation is the potential of the carrier in establishing strong electrostatic interactions between the negatively charged cell membranes and the positively charged CS/Bio-MOFs. The important point that is highlighted by Figure 17 is that 6 h incubation is not adequate for localization of the released DOX molecules in the cell nuclei so that the most intense signals of DOX refer to the cells' cytoplasm. However, 12 h of incubation seems sufficient, as it has led to the detection of highly intense DOX emissions from the nuclei. In this respect, it can be seen that prolonging the incubation time increases the intensity of intracellular red emissions. It should be noted that DOX release and accumulation in nuclei continues further, since the acidic media of the MCF-7 cells promote DOX release from the carrier and increase its efficiency, as the target of DOX resides within cell nuclei. In general, these results show that the DOX@CS/Bio-MOFs can diffuse into cytoplasm and release DOX, in addition to verifying that the released DOX molecules can reach the nuclei of cancerous cells to pose their anticancer effect. In this process, while DOX is released in a controlled manner within the target cells, the CS/Bio-MOFs are prohibited from diffusing into the nuclei since they are larger than the pores of cell nuclei.

Figure 18 shows the process of DOX@CS/Bio-MOF formation and its pH-responsive targeted drug delivery. When the pH is low, the CS chains swell in the medium and open the framework of the carrier. Upon this change, the loaded drug molecules can be easily released from the CS/Bio-MOFs. In contrast, at high pH, the CS chains are deprotonated and collapse to form a shielding layer on the surficial pores of the carrier. This conformational change leads to the blockage of the DOX@CS/Bio-MOF pores and restriction of drug release from them. Similarly, the Bio-MOFs coated by CS exhibit various conformations under a wide range of pH due to their diverse protonation states (see Figure 18).⁸² In this way, CS serves as a pH-responsive "channel controller", which ensures a higher extent of drug delivery at pH 6.8. At this pH, protonation of the amine groups allows the formation of a strong network of inter/intra CS chain hydrogen bonding, which holds the chains open in the "swollen" conformation and allows the DOX molecules to escape. Furthermore, the positive potential of CS/Bio-MOF, i.e. +33 mV, favors its cellular uptake.

4. CONCLUSION

In this work, a straightforward synthetic procedure was applied to modify the surface of Bio-MOF-13-Co by chitosan (CS) chains and use the resultant CS/Bio-MOF composite as a drug carrier. As a model drug, DOX was loaded into the prepared carrier under a slightly acidic condition (pH 6.8), which provided 92.5% drug loading efficiency. The obtained efficiency percentage was significantly higher than that of the unmodified Bio-MOF-13-Cos (76.0%). Also, during the in vitro studies, the percentage of DOX released from the CS/Bio-MOF carrier (93.0%) exceeded that of Bio-MOF-13-Co (54.1%) at pH 6.8 while the CS/Bio-MOF and Bio-MOF-13 samples respectively presented 45.0 and 48.3% DOX release at physiological pH (7.4). These results showed that surface modification of the carrier by CS allows a higher DOX loading and release under slightly acidic conditions, which are indicative of tumor cells, but a lower release rate at slightly higher pH levels, which are indicative of healthy cells. The mechanism involved was explained with respect to protonation of the CS amine groups at lower pH levels, which results in a strong network of inter/intrachain hydrogen bonding, holds the chains "open" in a swollen random coil conformation, and permits the loaded molecules to diffuse toward and away from the carrier. In contrast, at higher pH values, the amine groups of the CS chains deprotonate. Chain deprotonation results in breaking of the hydrogen-bonding network holding the chains in the swollen conformation, adopting a "closed" conformation and blocking the escape paths of the loaded molecules. In continuation of the in vitro studies, exposure of a breast cancer cell line, i.e. MCF-7, to the DOX-loaded carrier and free DOX demonstrated a substantially higher degree of cytotoxicity in the presence of the

Table 1. Quantitative Apoptosis Assay on the MCF-7 Cell Line Using the Annexin-V/PI Dual Staining Method in the Framework of the Flow Cytometry Method^a

treatment group	concn ($\mu\text{g mL}^{-1}$)	viable cells (Q4%)	early apoptotic cells (Q3%)	late apoptotic cells (Q2%)	necrotic cells (Q1%)	cell death	apoptotic cells (Q2% + Q3%)
control	3.125	76.5	0.519	16.6	6.42	23.53	17.11
CS/Bio-MOFs	3.125	76.2	2.27	14.1	7.47	23.84	16.37
free DOX	3.125	70.0	2.48	9.73	17.8	30.01	12.21
DOX@CS/Bio-MOFs	3.125	65.0	4.84	22.5	7.65	34.99	27.34

^aThe percentages of the viable, early apoptotic, late apoptotic, and necrotic cells are presented as mean values ($n = 3$).

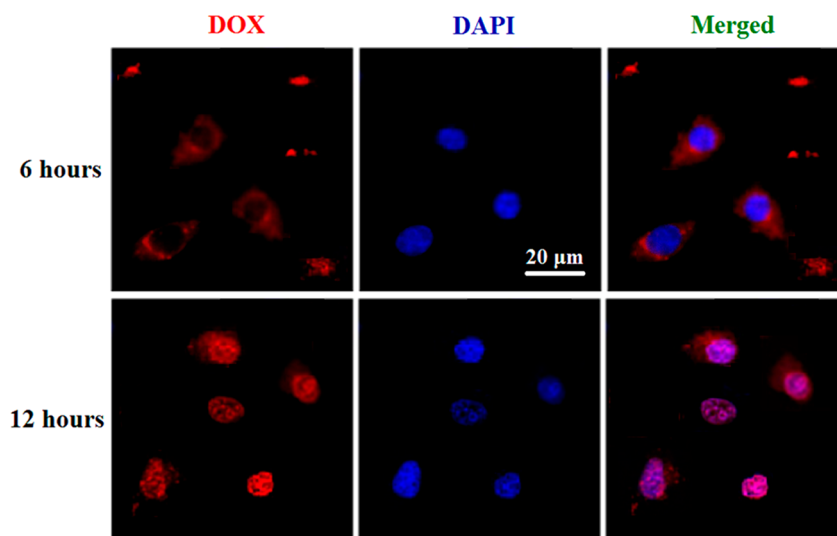


Figure 17. Fluorescence microscope images of the MCF-7 cells incubated with DOX@CS/Bio-MOF for 6 and 12 h.

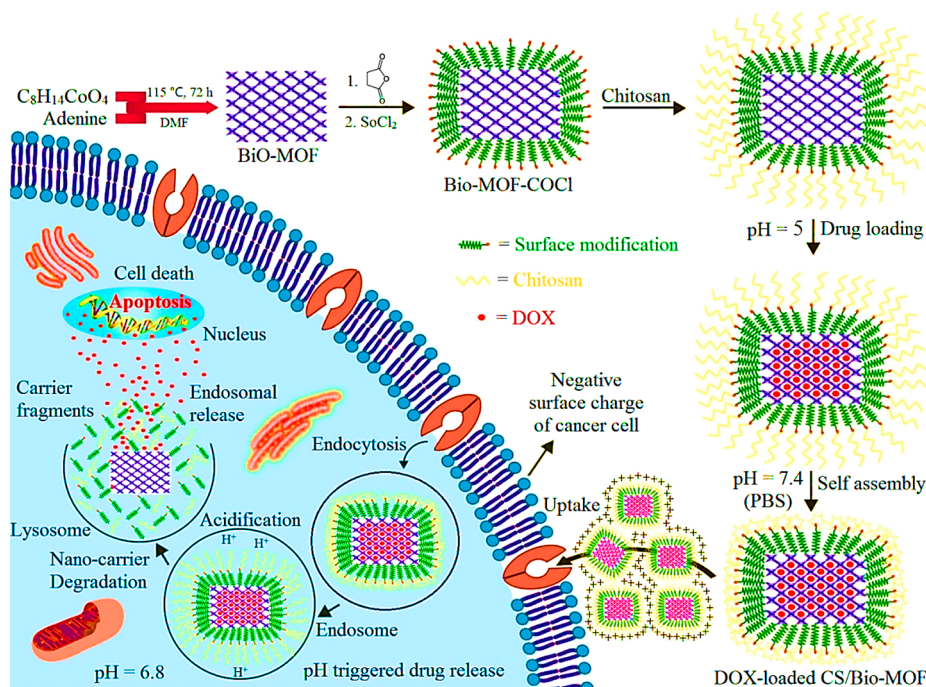


Figure 18. Schematic diagram of the DOX@CS/Bio-MOF formation and its drug release behavior at pH 6.8. The drug loading and conjugation processes of DOX@CS/Bio-MOF and illustration of the uptake and internalization of DOX@CS/Bio-MOF via an interaction and pH-triggered DOX release in lysosome or endosome of the MCF-7 cells.

DOX-loaded CS/Bio-MOF carrier in comparison with free DOX, at pH 6.8. The observed difference in cytotoxicity was attributed to both the slow release of DOX from the stable CS/Bio-MOF structure and increased diffusion of DOX through the cell walls as a result of CS biocompatibility. Further, flow cytometry and optical microscopy were used to assess the extent of apoptosis induced by the samples. The corresponding results, including the fluorescence microscopy images of the control and treated MCF-7 cells, clarified that the positively charged DOX-loaded CS/Bio-MOFs interact with the negatively charged cell membranes to diffuse into cancerous cells and release DOX, under the acidic condition of tumors. There, the released DOX molecules can localize in cell nuclei and induce apoptosis efficiently. In this way, the DOX-loaded CS/Bio-MOFs exhibit

the highest extent of cell apoptosis. In general, the *in vitro* studies showed that surface-modified Bio-MOF-13-Co can demonstrate superior specificity and cytotoxicity relative to the original material, in addition to acting as a pH-responsive carrier that can result in a greater efficacy in treatment of cancer with fewer side effects.

■ ASSOCIATED CONTENT

📄 Supporting Information

The Supporting Information is available free of charge on the ACS Publications website at DOI: 10.1021/acs.inorgchem.8b01955.

BET surface area, total pore volume, pore diameter, FE-SEM images, PXRD patterns, UV/vis absorption spectra

of the DOX release, and quantitative necrosis, apoptosis, and cell death assay for obtained materials (PDF)

AUTHOR INFORMATION

Corresponding Authors

*A.R.M.: tel, +98 2182883442; fax, +98 2182883455; e-mail, mahjouba@modares.ac.ir.

*F.A.: e-mail, ataei_f@modares.ac.ir.

*A.M.: e-mail, morsali_a@modares.ac.ir.

ORCID

Ali Reza Mahjoub: 0000-0002-2542-0031

Notes

The authors declare no competing financial interest.

ACKNOWLEDGMENTS

This work was supported by the Tarbiat Modares University, Iran. The authors are grateful for the financial support.

REFERENCES

- (1) Ulbrich, K.; Hola, K.; Šubr, V.; Bakandritsos, A.; Tucek, J.; Zboril, R. Targeted Drug Delivery with Polymers and Magnetic Nanoparticles: Covalent and Noncovalent Approaches, Release Control, and Clinical Studies. *Chem. Rev.* **2016**, *116*, 5338–5431.
- (2) Dong, Z.; Sun, Y.; Chu, J.; Zhang, X.; Deng, H. Multivariate Metal–Organic Frameworks for Dialing–in the Binding and Programming the Release of Drug Molecules. *J. Am. Chem. Soc.* **2017**, *139*, 14209–14216.
- (3) Cai, H.; Shen, T.; Kirillov, A. M.; Zhang, Y.; Shan, C.; Li, X.; Liu, W.; Tang, W. Self–Assembled Upconversion Nanoparticle Clusters for NIR–controlled Drug Release and Synergistic Therapy after Conjugation with Gold Nanoparticles. *Inorg. Chem.* **2017**, *56*, 5295–5304.
- (4) Calderera-Moore, M. E.; Liechty, W. B.; Peppas, N. A. Responsive Theranostic Systems: Integration of Diagnostic Imaging Agents and Responsive Controlled Release Drug Delivery Carriers. *Acc. Chem. Res.* **2011**, *44*, 1061–1070.
- (5) Song, Z.; Chen, X.; You, X.; Huang, K.; Dhinakar, A.; Gu, Z.; Wu, J. Self–Assembly of Peptide Amphiphiles for Drug Delivery: the Role of Peptide Primary and Secondary Structures. *Biomater. Sci.* **2017**, *5*, 2369–2380.
- (6) Zhang, Y.; Chang, Y.–Q.; Han, L.; Zhang, Y.; Chen, M.–L.; Shu, Y.; Wang, J.–H. Aptamer–Anchored Di–polymer Shell–Capped Mesoporous Carbon as a Drug Carrier for Bi–Trigger Targeted Drug Delivery. *J. Mater. Chem. B* **2017**, *5*, 6882–6889.
- (7) Fouladi, F.; Steffen, K. J.; Mallik, S. Enzyme–Responsive Liposomes for the Delivery of Anticancer Drugs. *Bioconjugate Chem.* **2017**, *28*, 857–868.
- (8) Carlino, L.; Rastelli, G. Dual Kinase–Bromodomain Inhibitors in Anticancer Drug Discovery: A Structural and Pharmacological Perspective. *J. Med. Chem.* **2016**, *59*, 9305–9320.
- (9) Kim, H. R.; You, D. G.; Park, S.–J.; Choi, K.–S.; Um, W.; Kim, J.–H.; Park, J. H.; Kim, Y.–S. MRI Monitoring of Tumor–Selective Anticancer Drug Delivery with Stable Thermosensitive liposomes Triggered by High–Intensity Focused Ultrasound. *Mol. Pharmaceutics* **2016**, *13*, 1528–1539.
- (10) Bellusci, M.; Guglielmi, P.; Masi, A.; Padella, F.; Singh, G.; Yaacoub, N.; Peddis, D.; Secci, D. Magnetic Metal–Organic Framework Composite by Fast and Facile Mechanochemical Process. *Inorg. Chem.* **2018**, *57*, 1806–1814.
- (11) Zheng, H.; Zhang, Y.; Liu, L.; Wan, W.; Guo, P.; Nyström, A. M.; Zou, X. One–Pot Synthesis of Metal–Organic Frameworks with Encapsulated Target Molecules and Their Applications for Controlled Drug Delivery. *J. Am. Chem. Soc.* **2016**, *138*, 962–968.
- (12) Teplensky, M. H.; Fantham, M.; Li, P.; Wang, T. C.; Mehta, J. P.; Young, L. J.; Moghadam, P. Z.; Hupp, J. T.; Farha, O. K.; Kaminski, C. F.; Fairen–Jimenez, D. Temperature Treatment of

Highly Porous Zirconium–Containing Metal–Organic Frameworks Extends Drug Delivery Release. *J. Am. Chem. Soc.* **2017**, *139*, 7522–7532.

(13) Alexander, C. M.; Maye, M. M.; Dabrowiak, J. C. DNA–Capped Nanoparticles Designed for Doxorubicin Drug Delivery. *Chem. Commun.* **2011**, *47*, 3418–3420.

(14) Tacar, O.; Sriamornsak, P.; Dass, C. R. Doxorubicin: an Update on Anticancer Molecular Action, Toxicity and Novel Drug Delivery Systems. *J. Pharm. Pharmacol.* **2013**, *65*, 157–170.

(15) Pan, U. N.; Khandelia, R.; Sanpui, P.; Das, S.; Paul, A.; Chattopadhyay, A. Protein–Based Multifunctional Nanocarriers for Imaging, Photothermal Therapy, and Anticancer Drug Delivery. *ACS Appl. Mater. Interfaces* **2017**, *9*, 19495–19501.

(16) Yang, X.; Du, H.; Liu, J.; Zhai, G. Advanced Nanocarriers Based on Heparin and its Derivatives for Cancer Management. *Biomacromolecules* **2015**, *16*, 423–436.

(17) Tagaya, M.; Ikoma, T.; Xu, Z.; Tanaka, J. Synthesis of Luminescent Nanoporous Silica Spheres Functionalized with Folic Acid for Targeting to Cancer Cells. *Inorg. Chem.* **2014**, *53*, 6817–6827.

(18) Cinay, G. E.; Erkoc, P.; Alipour, M.; Hashimoto, Y.; Sasaki, Y.; Akiyoshi, K.; Kizilel, S. Nanogel–Integrated pH Responsive Composite Hydrogels for Controlled Drug Delivery. *ACS Biomater. Sci. Eng.* **2017**, *3*, 370–380.

(19) Ma, L.; Lin, X.; Li, C.; Xu, Z.; Chan, C.–Y.; Tse, M.–K.; Shi, P.; Zhu, G. A Cancer Cell–Selective and Low–Toxic Bifunctional Heterodinuclear Pt(IV)–Ru(II) Anticancer Prodrug. *Inorg. Chem.* **2018**, *57*, 2917–2924.

(20) Li, B.; Meng, Z.; Li, Q.; Huang, X.; Kang, Z.; Dong, H.; Chen, J.; Sun, J.; Dong, Y.; Li, J.; Jia, X.; Sessler, J. L.; Meng, Q.; Li, C. A pH Responsive Complexation–Based Drug Delivery System for Oxaliplatin. *Chem. Sci.* **2017**, *8*, 4458–4464.

(21) Guan, X.; Guo, Z.; Wang, T.; Lin, L.; Chen, J.; Tian, H.; Chen, X. A pH–Responsive Detachable PEG Shielding Strategy for Gene Delivery System in Cancer Therapy. *Biomacromolecules* **2017**, *18*, 1342–1349.

(22) Maher, S.; Santos, A.; Kumeria, T.; Kaur, G.; Lambert, M.; Forward, P.; Evdokiou, A.; Losic, D. Multifunctional Microspherical Magnetic and pH Responsive Carriers for Combination Anticancer Therapy Engineered by Droplet–Based Microfluidics. *J. Mater. Chem. B* **2017**, *5*, 4097–4109.

(23) Xue, F.; Wen, Y.; Wei, P.; Gao, Y.; Zhou, Z.; Xiao, S.; Yi, T. A Smart Drug: a pH–Responsive Photothermal Ablation Agent for Golgi Apparatus Activated Cancer Therapy. *Chem. Commun.* **2017**, *53*, 6424–6427.

(24) Sun, X.; Du, R.; Zhang, L.; Zhang, G.; Zheng, X.; Qian, J.; Tian, X.; Zhou, J.; He, J.; Wang, Y.; Wu, Y.; Zhong, K.; Cai, D.; Zou, D.; Wu, Z. A pH–Responsive Yolk–Like Nanoplatfor for Tumor Targeted Dual–Mode Magnetic Resonance Imaging and Chemotherapy. *ACS Nano* **2017**, *11*, 7049–7059.

(25) Ellis, E.; Zhang, K.; Lin, Q.; Ye, E.; Poma, A.; Battaglia, G.; Loh, X. J.; Lee, T.–C. Biocompatible pH–Responsive Nanoparticles with a Core–Anchored Multilayer Shell of Triblock Copolymers for Enhanced Cancer Therapy. *J. Mater. Chem. B* **2017**, *5*, 4421–4425.

(26) Dai, Y.; Xu, C.; Sun, X.; Chen, X. Nanoparticle Design Strategies for Enhanced Anticancer Therapy by Exploiting the Tumour Microenvironment. *Chem. Soc. Rev.* **2017**, *46*, 3830–3852.

(27) Fan, W.; Yung, B.; Huang, P.; Chen, X. Nanotechnology for Multimodal Synergistic Cancer Therapy. *Chem. Rev.* **2017**, *117*, 13566–13638.

(28) Argyo, C.; Weiss, V.; Bräuchle, C.; Bein, T. Multifunctional Mesoporous Silica Nanoparticles as a Universal Platform for Drug Delivery. *Chem. Mater.* **2014**, *26*, 435–451.

(29) Zhao, Y.; Trewyn, B. G.; Slowing, I. I.; Lin, V. S.–Y. Mesoporous Silica Nanoparticle–Based Double Drug Delivery System for Glucose–Responsive Controlled Release of Insulin and Cyclic AMP. *J. Am. Chem. Soc.* **2009**, *131*, 8398–8400.

(30) Sun, Q.; You, Q.; Wang, J.; Liu, L.; Wang, Y.; Song, Y.; Cheng, Y.; Wang, S.; Tan, F.; Li, N. Theranostic Nanoplatfor: Triple–Model

Imaging Guided Synergistic Cancer Therapy Based on Liposomes Conjugated Mesoporous Silica Nanoparticles. *ACS Appl. Mater. Interfaces* **2018**, *10*, 1963–1975.

(31) Wu, M.-X.; Yang, Y.-W. Metal–Organic Framework (MOF)–Based Drug/Cargo Delivery and Cancer Therapy. *Adv. Mater.* **2017**, *29*, 1606134.

(32) Li, H.; Lv, N.; Li, X.; Liu, B.; Feng, J.; Ren, X.; Guo, T.; Chen, D.; Stoddart, F.; Gref, R.; Zhang, J. Composite CD–MOF Nanocrystals–Containing Microspheres for Sustained Drug Delivery. *Nanoscale* **2017**, *9*, 7454–7463.

(33) Gao, C.; Zheng, H.; Xing, L.; Shu, M.; Che, S. Designable Coordination Bonding in Mesopores as a pH–Responsive Release System. *Chem. Mater.* **2010**, *22*, 5437–5444.

(34) Huxford, R. C.; Della Rocca, J.; Lin, W. Metal–Organic Frameworks as Potential Drug Carriers. *Curr. Opin. Chem. Biol.* **2010**, *14*, 262–268.

(35) He, C.; Lu, K.; Liu, D.; Lin, W. Nanoscale Metal–Organic Frameworks for the Co–Delivery of Cisplatin and Pooled siRNAs to Enhance Therapeutic Efficacy in Drug–Resistant Ovarian Cancer Cells. *J. Am. Chem. Soc.* **2014**, *136*, 5181–5184.

(36) Horcajada, P.; Serre, C.; Maurin, G.; Ramsahye, N. A.; Balas, F.; Vallet-Regí, M.; Sebban, M.; Taulelle, F.; Ferey, G. Flexible Porous Metal–Organic Frameworks for a Controlled Drug Delivery. *J. Am. Chem. Soc.* **2008**, *130*, 6774–6780.

(37) Horcajada, P.; Serre, C.; Vallet-Regí, M.; Sebban, M.; Taulelle, F.; Ferey, G. Metal–Organic Frameworks as Efficient Materials for Drug Delivery. *Angew. Chem., Int. Ed.* **2006**, *45*, 5974–5978.

(38) Abazari, R.; Mahjoub, A. R.; Slawin, A. M. Z.; Carpenter-Warren, C. L. Morphology– and Size–Controlled Synthesis of a Metal–Organic Framework under Ultrasound Irradiation: An Efficient Carrier for pH Responsive Release of Anti–Cancer Drugs and Their Applicability for Adsorption of Amoxicillin from Aqueous Solution. *Ultrason. Sonochem.* **2018**, *42*, 594–608.

(39) Baati, T.; Njim, L.; Neffati, F.; Kerkeni, A.; Bouttemi, M.; Gref, R.; Najjar, M. F.; Zakhama, A.; Couvreur, P.; Serre, C.; Horcajada, P. In Depth Analysis of the *In Vivo* Toxicity of Nanoparticles of Porous Iron(III) Metal–Organic Frameworks. *Chem. Sci.* **2013**, *4*, 1597–1607.

(40) Abánades Lázaro, I.; Haddad, S.; Rodrigo-Muñoz, J. M.; Orellana-Tavra, C.; del Pozo, V.; Fairen-Jimenez, D.; Forgan, R. S. Mechanistic Investigation into the Selective Anticancer Cytotoxicity and Immune System Response of Surface–Functionalized, Dichloroacetate–Loaded, UiO–66 Nanoparticles. *ACS Appl. Mater. Interfaces* **2018**, *10*, 5255–5268.

(41) An, J.; Geib, S. J.; Rosi, N. L. Cation–Triggered Drug Release from a Porous Zinc–Adeninate Metal–Organic Framework. *J. Am. Chem. Soc.* **2009**, *131*, 8376–8377.

(42) McKinlay, A. C.; Morris, R. E.; Horcajada, P.; Frey, G.; Gref, R.; Couvreur, P.; Serre, C. Bio–MOFs: Metal–Organic Frameworks for Biological and Medical Applications. *Angew. Chem., Int. Ed.* **2010**, *49*, 6260–6266.

(43) Li, T.; Kozłowski, M. T.; Doud, E. A.; Blakely, M. N.; Rosi, N. L. Stepwise Ligand Exchange for the Preparation of a Family of Mesoporous MOFs. *J. Am. Chem. Soc.* **2013**, *135*, 11688–11691.

(44) Abazari, R.; Mahjoub, A. R.; Molaie, S.; Ghaffarifar, F.; Ghasemi, E.; Slawin, A. M. Z.; Carpenter-Warren, C. L. The Effect of Different Parameters under Ultrasound Irradiation for Synthesis of new Nanostructured Fe₃O₄@Bio–MOF as an Efficient Anti–Leishmanial *In Vitro* and *In Vivo* Conditions. *Ultrason. Sonochem.* **2018**, *43*, 248–261.

(45) Erucar, I.; Keskin, S. Efficient Storage of Drug and Cosmetic Molecules in Bio–compatible MOFs: A Molecular Simulation Study. *Ind. Eng. Chem. Res.* **2016**, *55*, 1929–1939.

(46) Doonan, C.; Riccò, R.; Liang, K.; Bradshaw, D.; Falcaro, P. Metal–Organic Frameworks at the Biointerface: Synthetic Strategies and Applications. *Acc. Chem. Res.* **2017**, *50*, 1423–1432.

(47) Gonzalez Miera, G.; Gómez, A. B.; Chupas, P. J.; Martín-Matute, B.; Chapman, K. W.; Platero-Prats, A. E. Topological

Transformation of a Metal–Organic Framework Triggered by Ligand Exchange. *Inorg. Chem.* **2017**, *56*, 4576–4583.

(48) Rojas, S.; Devic, T.; Horcajada, P. Metal Organic Frameworks Based on Bioactive Components. *J. Mater. Chem. B* **2017**, *5*, 2560–2573.

(49) Vasylevs'kyy, S. I.; Senchyk, G. A.; Lysenko, A. B.; Rusanov, E. B.; Chernega, A. N.; Jezierska, J.; Krautscheid, H.; Domasevitch, K. V.; Ozarowski, A. 1,2,4–Triazolyl–Carboxylate–Based MOFs Incorporating Triangular Cu(II)–Hydroxo Clusters: Topological Metamorphosis and Magnetism. *Inorg. Chem.* **2014**, *53*, 3642–3654.

(50) Rinaudo, M. Chitin and Chitosan: Properties and Applications. *Prog. Polym. Sci.* **2006**, *31*, 603–632.

(51) Wen, Y.; Yuan, Y.; Chen, H.; Xu, D.; Lin, K.; Liu, W. Effect of Chitosan on the Enantioselective Bioavailability of the Herbicide Dichlorprop to *Chlorella pyrenoidosa*. *Environ. Sci. Technol.* **2010**, *44*, 4981–4987.

(52) Nasr, F. H.; Khoei, S. Design, Characterization and *in vitro* Evaluation of Novel Shell Crosslinked poly(butylene adipate)–co–N–succinyl Chitosan Nanogels Containing Loteprednol Etabonate: A new System for Therapeutic Effect Enhancement via Controlled Drug Delivery. *Eur. J. Med. Chem.* **2015**, *102*, 132–142.

(53) Zhou, C.; Wang, M.; Zou, K.; Chen, J.; Zhu, Y.; Du, J. Antibacterial Polypeptide–Grafted Chitosan – Based Nanocapsules As an “Armed” Carrier of Anticancer and Antiepileptic Drugs. *ACS Macro Lett.* **2013**, *2*, 1021–1025.

(54) Zhou, H.; Yu, W.; Guo, X.; Liu, X.; Li, N.; Zhang, Y.; Ma, X. Synthesis and Characterization of Amphiphilic Glycidol–Chitosan–Deoxycholic Acid Nanoparticles as a Drug Carrier for Doxorubicin. *Biomacromolecules* **2010**, *11*, 3480–3486.

(55) Park, J. H.; Saravanakumar, G.; Kim, K.; Kwon, I. C. Targeted Delivery of Low Molecular Drugs using Chitosan and its Derivatives. *Adv. Drug Delivery Rev.* **2010**, *62*, 28–41.

(56) Fu, Y.–N.; Li, Y.; Li, G.; Yang, L.; Yuan, Q.; Tao, L.; Wang, X. Adaptive Chitosan Hollow Microspheres as Efficient Drug Carrier. *Biomacromolecules* **2017**, *18*, 2195–2204.

(57) Chowdhuri, A. R.; Singh, T.; Ghosh, S. K.; Sahu, S. K. Carbon Dots Embedded Magnetic Nanoparticles@Chitosan@Metal Organic Framework as a Nanoprobe for pH Sensitive Targeted Anticancer Drug Delivery. *ACS Appl. Mater. Interfaces* **2016**, *8*, 16573–16583.

(58) Islam, N.; Ferro, V. Recent Advances in Chitosan–Based Nanoparticulate Pulmonary Drug Delivery. *Nanoscale* **2016**, *8*, 14341–14358.

(59) Yang, X.–L.; Ju, X.–J.; Mu, X.–T.; Wang, W.; Xie, R.; Liu, Z.; Chu, L.–Y. Core–Shell Chitosan Microcapsules for Programmed Sequential Drug Release. *ACS Appl. Mater. Interfaces* **2016**, *8*, 10524–10534.

(60) Lv, G.; Qiu, L.; Liu, G.; Wang, W.; Li, K.; Zhao, X.; Lin, J. pH Sensitive Chitosan–Mesoporous Silica Nanoparticles for Targeted Delivery of a Ruthenium Complex with Enhanced Anticancer Effects. *Dalton Trans.* **2016**, *45*, 18147–18155.

(61) Justin, R.; Chen, B. Strong and Conductive Chitosan–Reduced Graphene Oxide Nanocomposites for Transdermal Drug Delivery. *J. Mater. Chem. B* **2014**, *2*, 3759–3770.

(62) Wang, Y.; Pitto-Barry, A.; Habtemariam, A.; Romero-Canelon, I.; Sadler, P. J.; Barry, N. P. E. Nanoparticles of Chitosan Conjugated to Organoruthenium Complexes. *Inorg. Chem. Front.* **2016**, *3*, 1058–1064.

(63) Li, T.; Chen, D.–L.; Sullivan, J. E.; Kozłowski, M. T.; Johnson, J. K.; Rosi, N. L. Systematic Modulation and Enhancement of CO₂ N₂ Selectivity and Water Stability in an Isorectical Series of Bio–MOF–11 Analogues. *Chem. Sci.* **2013**, *4*, 1746–1755.

(64) Kalliola, S.; Repo, E.; Srivastava, V.; Heiskanen, J. P.; Antti Sirviö, J.; Liimatainen, H.; Sillanpää, M. The pH Sensitive Properties of Carboxymethyl Chitosan Nanoparticles Cross–Linked with Calcium Ions. *Colloids Surf., B* **2017**, *153*, 229–236.

(65) Zhao, X.; Wei, Z.; Zhao, Z.; Miao, Y.; Qiu, Y.; Yang, W.; Jia, X.; Liu, Z.; Hou, H. Design and Development of Graphene Oxide Nanoparticle/Chitosan Hybrids Showing pH–Sensitive Surface

Charge-Reversible Abili600ty for Efficient Intracellular Doxorubicin Delivery. *ACS Appl. Mater. Interfaces* **2018**, *10*, 6608–6617.

(66) Yang, Q.; Wang, S.; Fan, P.; Wang, L.; Di, Y.; Lin, K.; Xiao, F.—S. pH-Responsive Carrier System Based on Carboxylic Acid Modified Mesoporous Silica and Polyelectrolyte for Drug Delivery. *Chem. Mater.* **2005**, *17*, 5999–6003.

(67) Dong, B.; Song, X.; Kong, X.; Wang, C.; Zhang, N.; Lin, W. A Tumor-Targeting and Lysosome-Specific Two-Photon Fluorescent Probe for Imaging pH Changes in Living Cells. *J. Mater. Chem. B* **2017**, *5*, 988–995.

(68) Shaibani, P. M.; Etayash, H.; Naicker, S.; Kaur, K.; Thundat, T. Metabolic Study of Cancer Cells Using a pH Sensitive Hydrogel Nanofiber Light Addressable Potentiometric Sensor. *ACS Sens.* **2017**, *2*, 151–156.

(69) Ren, Y.; Abbood, H. A.; He, F.; Peng, H.; Huang, K. Magnetic EDTA-Modified chitosan/SiO₂/Fe₃O₄ Adsorbent: Preparation, Characterization, and Application in Heavy Metal Adsorption. *Chem. Eng. J.* **2013**, *226*, 300–311.

(70) Neufeld, M. J.; Lutzke, A.; Tapia, J. B.; Reynolds, M. M. Metal-Organic Framework/Chitosan Hybrid Materials Promote Nitric Oxide Release from S-Nitrosoglutathione in Aqueous Solution. *ACS Appl. Mater. Interfaces* **2017**, *9*, 5139–5148.

(71) Zhang, L.; Sun, J.; Zhou, Y.; Zhong, Y.; Ying, Y.; Li, Y.; Liu, Y.; Zuhra, Z.; Huang, C. Layer-by-Layer Assembly of Cu₃(BTC)₂ on Chitosan Non-Woven Fabrics: a Promising Haemostatic Decontaminant Composite Material Against Sulfur Mustard. *J. Mater. Chem. B* **2017**, *5*, 6138–6146.

(72) Saputra, E.; Muhammad, S.; Sun, H.; Ang, H.—M.; Tadé, M. O.; Wang, S. Manganese Oxides at Different Oxidation States for Heterogeneous Activation of Peroxymonosulfate for Phenol Degradation in Aqueous Solutions. *Appl. Catal., B* **2013**, *142–143*, 729–735.

(73) Azhar, M. R.; Abid, H. R.; Sun, H.; Periasamy, V.; Tadé, M. O.; Wang, S. One-Pot Synthesis of Binary Metal Organic Frameworks (HKUST-1 and UiO-66) for Enhanced Adsorptive Removal of Water Contaminants. *J. Colloid Interface Sci.* **2017**, *490*, 685–694.

(74) Terada, D.; Kobayashi, H.; Zhang, K.; Tiwari, A.; Yoshikawa, C.; Hanagata, N. Transient Charge-Masking Effect of Applied Voltage on Electrospinning of Pure Chitosan Nanofibers from Aqueous Solutions. *Sci. Technol. Adv. Mater.* **2012**, *13*, 015003.

(75) Rahmani, S.; Mohammadi, Z.; Amini, M.; Isaei, E.; Taheritargh, S.; Tehrani, N. R.; Tehrani, M. R. Methylated 4-N,N Dimethyl Aminobenzyl N,O Carboxymethyl Chitosan as a New Chitosan Derivative: Synthesis, Characterization, Cytotoxicity and Antibacterial Activity. *Carbohydr. Polym.* **2016**, *149*, 131–139.

(76) Chan, P.; Kurisawa, M.; Chung, J. E.; Yang, Y.—Y. Synthesis and Characterization of Chitosan-g-Poly(Ethylene Glycol)-Folate as a Non-Viral Carrier for Tumor-Targeted Gene Delivery. *Biomaterials* **2007**, *28*, 540–549.

(77) Tai, S.; Zhang, W.; Zhang, J.; Luo, G.; Jia, Y.; Deng, M.; Ling, Y. Facile Preparation of UiO-66 Nanoparticles with Tunable Sizes in a Continuous Flow Microreactor and its Application in Drug Delivery. *Microporous Mesoporous Mater.* **2016**, *220*, 148–154.

(78) Bhattarai, N.; Gunn, J.; Zhang, M. Chitosan-Based Hydrogels for Controlled, Localized Drug Delivery. *Adv. Drug Delivery Rev.* **2010**, *62*, 83–99.

(79) Wu, B. J.; Sailor, M. J. Chitosan Hydrogel-Capped Porous SiO₂ as a pH Responsive Nano-Valve for Triggered Release of Insulin. *Adv. Funct. Mater.* **2009**, *19*, 733–741.

(80) Song, S. W.; Hidajat, K.; Kawi, S. pH-Controllable Drug Release using Hydrogel Encapsulated Mesoporous Silica. *Chem. Commun.* **2007**, *1*, 4396–4398.

(81) Sorlier, P.; Viton, C.; Domard, A. Relation between Solution Properties and Degree of Acetylation of Chitosan: Role of Aging. *Biomacromolecules* **2002**, *3*, 1336–1342.

(82) Popat, A.; Liu, J.; Lu, G. Q. M.; Qiao, S. Z. A pH Responsive Drug Delivery System Based on Chitosan Coated Mesoporous Silica Nanoparticles. *J. Mater. Chem.* **2012**, *22*, 11173–11178.

(83) Abazari, R.; Mahjoub, A. R. Potential Applications of Magnetic β -AgVO₃/ZnFe₂O₄ Nanocomposites in Dyes, Photocatalytic Degradation, and Catalytic Thermal Decomposition of Ammonium Perchlorate. *Ind. Eng. Chem. Res.* **2017**, *56*, 623–634.

(84) Barick, K. C.; Nigam, S.; Bahadur, D. Nanoscale Assembly of Mesoporous ZnO: A Potential Drug Carrier. *J. Mater. Chem.* **2010**, *20*, 6446–6452.

(85) Vimala, K.; Shanthi, K.; Sundarraj, S.; Kannan, S. Synergistic Effect of Chemo-Photothermal for Breast Cancer Therapy Using Folic Acid (FA) Modified Zinc Oxide Nanosheet. *J. Colloid Interface Sci.* **2017**, *488*, 92–108.

(86) Napierska, D.; Thomassen, L. C. J.; Rabolli, V.; Lison, D.; Gonzalez, L.; Kirsch-Volders, M.; Martens, J. A.; Hoet, P. H. Size-Dependent Cytotoxicity of Monodisperse Silica Nanoparticles in Human Endothelial Cells. *Small* **2009**, *5*, 846–853.

(87) Chen, T.; Liu, Y.; Zheng, W.—J.; Liu, J.; Wong, Y.—S. Ruthenium Polypyridyl Complexes That Induce Mitochondria-Mediated Apoptosis in Cancer Cells. *Inorg. Chem.* **2010**, *49*, 6366–6368.

(88) Wang, L.; Zhou, B.—B.; Yu, K.; Su, Z.—H.; Gao, S.; Chu, L.—L.; Liu, J.—R.; Yang, G.—Y. Novel Antitumor Agent, Trilacunary Keggin-Type Tungstobismuthate, Inhibits Proliferation and Induces Apoptosis in Human Gastric Cancer SGC-7901 Cells. *Inorg. Chem.* **2013**, *52*, 5119–5127.